Thermal Modeling for Pulsed Inductive FRC Plasmoid Thrusters

Michael Pfaff

A thesis submitted in partial fulfillment of

the requirements for the degree of

Master of Science in Aeronautics & Astronautics

University of Washington

2013

Committee:

John Slough

David Kirtley

Program Authorized to Offer Degree

Aeronautics & Astronautics

University of Washington

Abstract

Thermal Modeling for Pulsed Inductive FRC Plasmoid Thrusters

Michael Pfaff

Chair of the Supervisory Committee:
Professor John Slough
Department of Aeronautics and Astronautics

Due to the rising importance of space based infrastructure, long-range robotic space missions, and the need for active attitude control for spacecraft, research into Electric Propulsion is becoming increasingly important. Electric Propulsion (EP) systems utilize electric power to accelerate ions in order to produce thrust. Unlike traditional chemical propulsion, this means that thrust levels are relatively low. The trade-off is that EP thrusters have very high specific impulses (I_{sp}), and can therefore make do with far less onboard propellant than cold gas, monopropellant, or bipropellant engines. As a consequence of the high power levels used to accelerate the ionized propellant, there is a mass and cost penalty in terms of solar panels and a power processing unit. Due to the large power consumption (and waste heat) from electric propulsion thrusters, accurate measurements and predictions of thermal losses are needed. Excessive heating in sensitive locations within a thruster may lead to premature failure of vital components. Between the fixed cost required to purchase these components, as well as the man-hours needed to assemble (or replace) them, attempting to build a high-power thruster without reliable thermal modeling can be expensive. This paper will explain the usage of FEM modeling and experimental tests in characterizing the ElectroMagnetic Plasmoid Thruster (EMPT) and the Electrodeless Lorentz Force (ELF) thruster at the MSNW LLC facility in Redmond, Washington. The EMPT thruster model is validated using an experimental setup, and steady state temperatures are predicted for vacuum conditions. Preliminary analysis of the ELF thruster indicates possible material failure in absence of an active cooling system for driving electronics and for certain power levels.

Table of Contents

List of Figures

List of Tables

Chapter 1: Introduction

1.1 Propulsion

For attitude control and long range space missions, the benefits of EP are incredible. Using the Tsiolkovsky rocket equation below, it can be seen that the total mass fraction (and thus, the propellant mass) for a given velocity change (ΔV) will decrease exponentially as specific impulse grows. This implies that, for long range missions where system mass is more important than power availability, electric propulsion benefit. For missions with an extreme ΔV change, such as a mission to an asteroid or comet, electric propulsion may provide the sole solution for propulsion.

Equation 1

$$\frac{m_{initial}}{m_{final}} = e^{\frac{I_{sp} g_0}{\Delta V}}$$

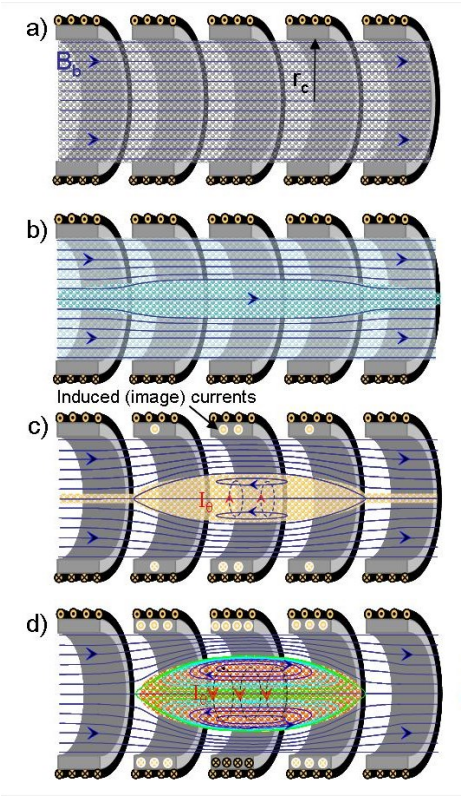

Figure 1. FRC formation in a cylindrical geometry [10]

Electric Propulsion thrusters are divided into several different categories by the mechanism used to accelerate the ionized propellant. Magnetoplasmadynamic (MPD) thrusters use the combination of current density from moving electrons and a perpendicular magnetic field create a jxB force on charged ions, known as the Lorentz force. This combination of current and magnetic field classifies these thrusters as "electromagnetic," or needing both an electric field and a magnetic field to function. On the

other hand, “electrostatic” thrusters such as ion engines use a gridded array charged opposite to the ions, such that they are accelerated toward the grid and out of the thruster. This force is known as the Coulomb force and is proportional to the magnitude of the ion charge multiplied by the grid charge. Another common electrostatic type is the Hall Effect thruster, which uses a cylindrical anode and cathode to confine and accelerate plasma.

The primary method for thrust production that will be discussed in this thesis is the use of a Field Reverse Configuration (FRC) plasmoid. Thrusters that use FRC’s are electromagnetic due to the nature of accelerating the plasmoids. In Figure 1 the formation of an FRC is illustrated as a four step process.

- In step (a), bias coils are used to create a steady axial B field.
- In step (b), lightly ionized gas is injected into this magnetic field. Two pairs of antenna coils oriented 90 degrees from each other and operated 90 degrees out of phase from one another then start to drive an oscillating current. This causes a rotating magnetic field (RMF) to be generated. The electrons in the injected gas are attached to the magnetic field lines and fully ionize the plasma.
- This rotation also generates the azimuthal current shown in step (c). As a result, this creates a second (blue) axial magnetic field around the current that confines the plasma.
- As the plasma becomes fully ionized and the electrons become fully attached to the RMF, the structure known as the Field Reverse Configuration plasmoid shown in step (d) is formed. During this process conducting rings around the thruster act to conserve flux and provide a radial pressure balance to the FRC.

The plasmoid is then ejected via the electromagnetic Lorentz force caused by the cross between the azimuthal plasma current and radial component of the bias field. When combined with a magnetic field gradient force from a conical thruster geometry, the FRC can be thermally expanded out of the cone to produce thrust. The ejection of an FRC from an EMPT thruster variant is shown as Figure 2 below.

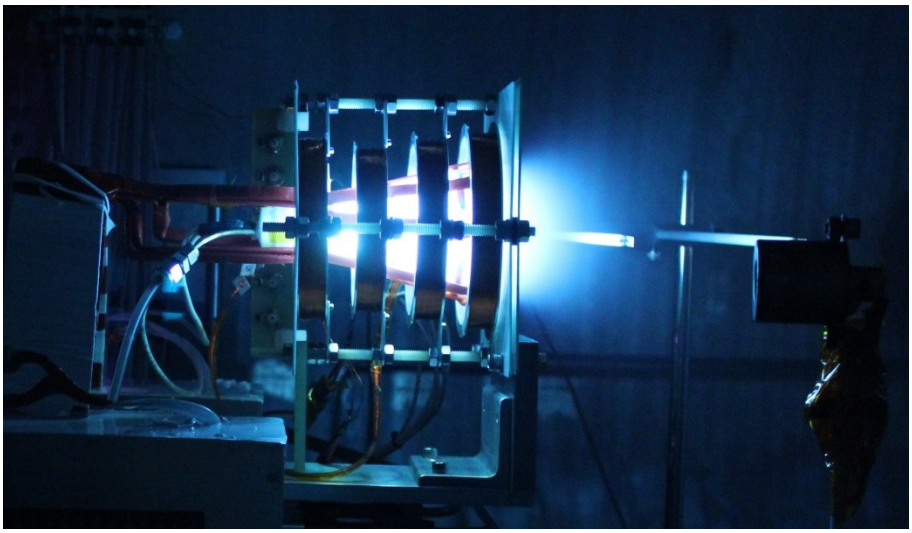

Figure 2. Ejection of an FRC from EMPT, showing the conical geometry of the thruster

Using MSNW's methods for generating FRC plasmoids as propulsion can alleviate some of the problems that trouble traditional thruster development. Due to plasma interaction with the walls of the thruster, most engine types require exotic materials to withstand the high temperature loading. Due to the magnetic confinement of the FRC, the plasma does not interact with or transfer heat to the walls. This ensures that heat loading to the inside of the cone is far less than that of the traditional EP thrusters. The main sources of heating are therefore:

- Radiative energy from the FRC on the inside of the cone
- Ohmic heating in the rotating magnetic field (RMF) coils
- Ohmic heating in the bias coils
- Induced heating in the aluminum flux conservers
- Heat generated by the integrated power supply system components

At low power levels (several kilowatts), the heat generated by these components is relatively small compared to the heat sinkable area of the thruster and the primary concern is thermal interaction with electronics and power processing equipment. However, as the power level is scaled up for larger thrusters, heat management of the thruster itself does become an issue.

1.2 Thermal

In order to understand the processes by which an electromagnetic thruster's thermal characteristics can be analyzed, it is important to understand the underlying concepts behind heat transfer and thermal processes. There are three methods of heat transfer within a system. First, conduction represents surface to surface contact between two solid materials. In this case, conductivity defines the heat flow between different materials and components in the thrusters. The molecules of each material have a certain energy based off of the temperature of the solid they represent. Over time the energy difference between the two solids will equalize across the interface between them and the system will reach equilibrium. The rate (for a one dimensional system) at which this occurs is based off of the temperature gradient between the two materials, a characteristic length (thruster height), and what is known as the conductivity constant. This relationship, Fourier's Law, is shown in Equation 2 [1]. The conductivity constant has units of W/m^2 and represents how well the molecules within the solid matrix of the material will transfer their energy within that matrix (AKA, the same material). This implies that, while uncommon, a 3-dimensional material can have an "orthotropic," or non-spatially uniform heat conductivity.

Equation 2

$$\dot{q} = -k\nabla T$$

Second, convection represents the energy transfer between a fluid and another material, whether that material is solid or another fluid. There are two mechanisms that make up the convection process. Natural convection (diffusion), or heat transfer by the random motion of molecules composing the fluid, is one process. The other is the velocity or overall bulk motion of the fluid, which also contributes to the

convection term. [1] This term is readily affected by characteristics of the fluid and system such as turbulent vs. laminar flow, or boundary layer thickness. Similar to conduction, the rate at which energy is transferred via convection is due to a temperature difference and by a convection constant to the surrounding fluid. This is shown in Equation 3 [1], where the heat transfer rate is in units of $W/m^2 \cdot K$. It should be noted that determining the exact convection constant in a real-life experiment is difficult due to the chaotic nature of fluid flow. In an open-air laboratory experiment, convection cooling is the dominant form of heat transfer from the thruster.

Equation 3

$$\dot{q} = h(T_{surface} - T_{ambient})$$

The third and final method of heat transfer is via thermal radiation. A material at any temperature above 0 Kelvin will naturally produce electromagnetic thermal radiation according to the Stephan-Boltzmann law, shown in Equation 4. From this relationship, it is obvious that the power emitted by an object scales very quickly with temperature due to the fourth power. The σ in the equation represents a constant, but the ϵ is a fractional variable that represents the emissivity of a given surface. Emissivity ranges from 0 to 1 and represents the ability of a surface to emit power to its surroundings. Radiation is the typical cooling mechanism for a space propulsion system in a vacuum chamber or in space.

Equation 4

$$P = A\epsilon\sigma {T_{surface}}^4$$

Emissivity is a difficult variable to determine, as it is based off of surface characteristics such as color, roughness, temperature, and viewing angle. For the most part, a constant average emissivity value can be used for thermal calculations within a relatively small wavelength and temperature range. Due to the specialized nature of equipment to determine emissivity, it often falls to using emissivity tables and calibration experiments beforehand in order to reach the correct value as was done in this program.

Complementary to emissivity is the variable α, which represents the ability of a surface to absorb heat from an incoming source. This leads to an energy balance equation in which the rate of heat into or out of a system is determined by the thermal energy it emits versus that which it absorbs from its surroundings. This energy balance is illustrated in Equation 5.

Equation 5

$$P = \epsilon\sigma {T_{surface}}^4 - \alpha\sigma {T_{surroundings}}^4$$

1.3 Consequences

Practically speaking, it is far more difficult to test an experimental thruster in vacuum than it is in air. Not only are there arcing problems to deal with, but heating is a much more difficult problem. Typically, convection in air off of an object will dominate any effects of radiation, essentially reducing it to a

second order term. However, in a vacuum there are no fluids to transfer the heat of the thruster to, and so it will generally become much hotter than an in-air test.

There are several other consequences of these heating processes, especially in vacuum. As different materials on the thruster begin to heat, they begin to outgas. This means that the vacuum chamber and equipment within the vacuum chamber can be exposed to water vapor, CO2, and different organic volatiles. This could potentially damage them just as it could damage sensitive instrumentation onboard a spacecraft. As such, it is best to use low outgassing materials in high temperature locations. Additionally, with high electric power thrusters, outright material failure or melting can occur if the temperature becomes too high. For example, most metals will withstand extremely high temperatures before softening. Aluminum and Copper each have softening points of 582°C and 1010°C, respectively. In contrast, Teflon based "Tefzel" wire sheathing will fail at 255°C, and Nylon will fail at 100°C. This means that to ensure that all materials are adequately protected from adverse thermal conditions, tests need to be performed to examine the temperature distribution across the thruster.

1.4 Finite Element Analysis

The following analyses in this thesis were performed using the finite element modeling (FEM) program ANSYS® Academic Research, Release 14. This particular section will instead focus on reviewing the underlying concepts behind the thermal solvers that ANSYS® uses to form a solution.

A finite element program is innately designed around breaking up a large problem (a complex 3D model) into smaller, more manageable chunks, an example of which is shown in Figure 3. Each chunk, or element, may have different material characteristics. It may also consist of different shapes and sizes, depending on the meshing technique used. Partial differential equations reflecting the time and space variability of the processes in question (in this case, thermal processes) are solved simultaneously for each of these elements, as each element affects the elements around it. However, as the number of elements in a model increases, this increases the number of partial differential equations that must be solved. This results in high resolution (low element size) models requiring large amounts of computational power and/or long periods of time for a solution. As a result, meshing algorithms that can maintain solution accuracy while ensuring low total element numbers are relatively important to a FEM program. The specific techniques behind meshing a 3D model in this way are not within the scope of this paper, but can be researched elsewhere.

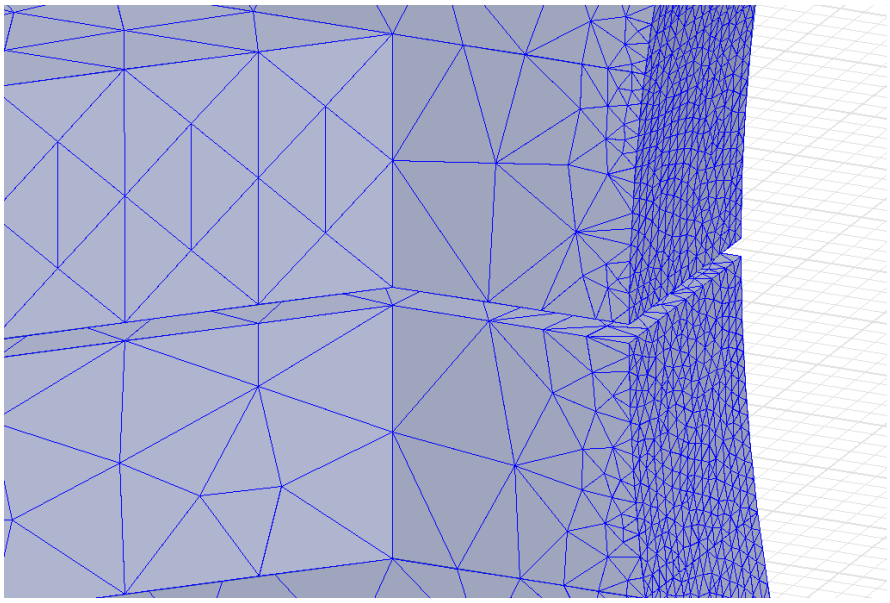

Figure 3. Automatically generated mesh grid showing increased resolution (decreased element size) on area of interest; in this case, a magnet with a surface current along the inside edge in an electromagnetic FEM solver.

In addition to the fidelity of the mesh grid, the solver type can also affect the accuracy of the solution. There are two primary types of thermal solvers that can be used, depending on the requirements of the end-user. First, the Steady State Thermal solver can be used to find the equilibrium solution for a model with a given set of heat sources and sinks. Second, the Transient Thermal solver can be used to determine temperature across a model at discrete time steps.

The Steady State Thermal solver works off of the equilibrium Equation 6 below [2].

Equation 6

$$[K]\{T\} = \{Q_{heat\ flow} + Q_{heat\ flux} + Q_{heat\ generation} + Q_{covection} + Q_{radiation}\}$$

In this equation, [K] represents the conductivity matrix for the model. That is to say, when a model is meshed, each element within the mesh has a certain conductivity assigned to it based off of the material of which the mesh element is composed. {T} is a matrix that represents the temperature values at each element. On the right side of the equation, the different Q's represent different sources and sinks for each element value. Some will be 0, such as the radiation or convection term on an internal model element. Others are based off of the geometry setup, such as the heat generation term, which is usually assigned to specific heat sources within a model.

The Transient Thermal solver uses Equation 7 below [2].

Equation 7

$$[C]\{\dot{T}\} + [K]\{T\} = \{Q_{heat\ flow} + Q_{heat\ flux} + Q_{heat\ generation} + Q_{covection} + Q_{radiation}\}$$

This differential equation is similar to the Steady State Thermal solver except that there has been a temperature rate added on the left side. This is multiplied by the matrix [C], which represents the specific heat at each element in the model. As opposed to Equation 6, this must be solved in a stepwise manner with respect to time. This stepwise equation is shown below as Equation 8, where the n subscripts denote a time, t_n. The n+1 subscripts therefore represent the values at one timestep forward in time [2].

Equation 8

$$\{T_{n+1}\} = \{T_n\} + (1-\theta)\Delta t\{\dot{T}_n\} + \theta\Delta t\{\dot{T}_{n+1}\}$$

Several different variables are involved in controlling the convergence and characteristics of the differential equation. Each $\{T_i\}$ represents the matrix of temperatures across all elements in the model at that time. The Δt represents the timestep used by the program. θ is a "transient integration parameter" (TIP) used to control the convergence/precision of the equation. A smaller TIP might force the solution to converge quicker, but might result in unwanted oscillations or complete divergence in the solution. The $\dot{T}$, in turn, represents the time rate of temperature changes within each element. This presents a problem, however, in that the time rate of change for the next time step is not known ahead of time. Thus, Equation 8 is solved for $\dot{T}_{N+1}$ and substituted into Equation 7 at t_{n+1}. The resulting Equation 9 can be solved for T_{n+1}, which can then be substituted back into Equation 8 in order to find $\dot{T}_{n+1}$. The next timestep, $\dot{T}_{n+1}$, becomes $\dot{T}_n$ and the process begins again [2].

Equation 9

$$\left(\frac{1}{\theta\Delta t}[C] + [K]\right)\{T_{n+1}\} - [C]\left(\frac{1}{\theta\Delta t}\{T_n\} + \frac{1-\theta}{\theta}\{\dot{T}_n\}\right) = \sum Q_{heating}$$

There are several real-life effects that these models do not account for. All three methods of heat transfer are technically dependent on the temperature of the body in question as well as the ambient energy of the outside medium (fluid temperature or radiation in vacuum). The implication is that the average emissivity, the thermal conductivity constant, and the convection constant are only constants at a specific temperature. As temperature increases, emissivity will also tend to increase, but the temperature change required to see more than a minute change in the value of the constant is on the order of hundreds to thousands of Kelvin, so it is treated as a constant. However, the same is not true for the convection constant.

The convection constant is heavily reliant on the fluid characteristics of the air around the object, such as buoyancy, fluid viscosity, and gravitational effects. Several different empirical formulas have been developed to model the convection constant in simplistic cases, such as a horizontal or vertical planar wall. Since the EMPT thruster discussed in this paper has its heat sinking surfaces aligned primarily in the vertical direction as shown later in Figure 7, the empirical vertical plate correlation in Equation 10 by Churchill and Chu may be used [3].

Equation 10

$$h_{laminar} = \frac{k}{L}\left(0.68 + \frac{0.670 Ra_L^{\frac{1}{4}}}{\left[1 + \left(\frac{0.492}{\mathrm{Pr}}\right)^{\frac{9}{16}}\right]^{\frac{4}{9}}}\right)$$

This equation assumes a laminar flow and that the Raleigh number is less than 10^9. For the characteristic length (height) of the thruster, L, and general temperatures that the thruster performs at, this is a reasonable assumption. This also assumes that the only convection on the thruster is natural convection, thus the velocity of the ambient air is zero. This equation is important to note because the Raleigh number (Ra) changes based off of the difference between the surface temperature and the ambient air, as show below in Equation 11. β is the thermal expansion coefficient of the fluid (air), g is the gravitational constant, ν is the kinematic viscosity of the fluid, and α is the thermal diffusivity. The important constants are both T_s and T_∞, which represent the surface temperature and ambient fluid temperature, respectively. The constant x represents the characteristic length of the vertical surface in question [1].

Equation 11

$$Ra = \frac{g\beta(T_s - T_\infty)x^3}{\nu\alpha}$$

While both g and β are defined independent of temperature, the kinematic viscosity and thermal diffusivity are slightly more complicated. Both Equation 12 and Equation 13 illustrate their dependence on density, in addition to thermal conductivity k, specific heat capacity c_p, and dynamic viscosity μ. As is clear through the ideal gas law, both of these values will proportionally change with changing temperature.

Equation 12

$$\alpha = \frac{k}{\rho c_p}$$

Equation 13

$$\nu = \frac{\mu}{\rho}$$

In addition to the Raleigh number, the Prandtl number also plays a significant role in determining the convection coefficient. The Prandtl number is based off of Equation 12 and Equation 13 and is displayed below as Equation 14. Clearly, the Prandtl number is not based off of the density of the surrounding fluid, and so is not variable with temperature.

Equation 14

$$Pr = \frac{\nu}{\alpha}$$

It is important to define how the convection constant changes as a function of temperature due to the time-stepping process ANSYS® must perform to solve the FEM problem. Since the $Q_{convection}$ on the right side of Equation 9 is now a function of temperature, a new method must be used to solve the problem. This method is known as the Newton-Raphson iterative procedure. This iterative method requires that the solution for a given time step converges to an equilibrium value. An example of this is shown in Equation 15. This equation illustrates how the change in temperature experienced across the different elements of the model (the K conductivity matrix) is equal to the difference between the applied thermal load vector and a thermal resistance heat flow vector. This difference is essentially the residual load vector, or the amount that the system is out of equilibrium [2].

Equation 15

$$\left[K_i^{Tangent}\right]\{\Delta T_i\} = \{F^a\} - \{F_i^{nr}\}$$

The algorithm starts at an initial temperature defined by either the previous step or by user-input from ANSYS®. The conductivity matrix and restoring load can then be calculated through traditional methods. Note that the conductivity matrix and restoring load may change significantly each time the initial temperature does as the load vector (convection term) is temperature dependent. Once both have been calculated, Equation 15 is used to find the ΔT_i. Another equation must then be used to find the next guess at the equilibrium temperature [2].

Equation 16

$$\{T_{i+1}\} = \{T_i\} + \{\Delta T_i\}$$

Using Equation 16, the old T_i becomes the initial guess for Equation 15 and the cycle starts again. This will cause the ΔT_i to decrease and for the solution to converge to a final value over several time steps. After a converged solution is found, the solver can advance to the next timestep. Computationally, this method is the most time consuming, as it adds another convergence method to solve before a solution can be found. However, this method may also be utilized to determine a solution if temperature dependent thermal conductivity values or emissivities are specified.

1.5 Thermal Modeling Background in Electric Propulsion

Being able to characterize the thermal characteristics of a propulsion system is critically important for operation in vacuum conditions. Without natural convection to rely upon, thrusters will quickly heat up and destroy vital components if they are not properly heat sunk. Several examples of the necessity of this are now shown.

Hall thrusters, mentioned previously, have been in use for many years as attitude control mechanisms onboard spacecraft. The Busek BHT-200, a 200 Watt Hall thruster, is an example of a flight ready engine that had extensive thermal measurements performed on it during steady state firing. The BHT-200 was launched in December of 2006 onboard the TacSat-2 test bed satellite by the Orbital Sciences Corporation [4]. Due to the required proximity of the Hall thruster anode to the plasma, experiments performed at the Air Force Research Laboratory indicated that the anode would peak at approximately 375°C during steady operation [5]. Incidentally, this extraordinarily high temperature forces the manufacturer of the Hall thruster into using exotic metals like boron nitride or ceramics. Further testing indicated that as power/propellant flow rate increased, temperature also increased, albeit at a decreasing rate. This was shown by tests performed on a 600 Watt Busek BHT-600 that peaked at approximately 450°C [5].

Another thruster type examined for use on spacecraft is a gridded ion thruster. Since the grid is biased in order to attract and propel plasma out the rear of the thruster, naturally some of these ions impact against the grid, causing sputtering and transferring energy in the form of heat into the thruster body. The NASA Evolutionary Xenon Thruster (NEXT) has undergone significant experimental and theoretical testing, and so is an excellent illustration of the heat distribution of an ion thruster. With a discharge power of 434 Watts (the highest setting tested) the main front section of the thruster body reached 249°C. [6] Meanwhile, the cathode tube (for ionizing the gas) and the graphite keeper used to neutralize the plasma spray post acceleration reached 459°C and 563°C, respectively [6].

Much of the heating in these engines is due to direct interaction between the plasma and the structure of the thruster, a problem that an FRC based thruster does not have due to the bias field preventing the ionized plasma from reaching the walls. Thus, a 1 kW thruster utilizing FRC technology would have most of its heating come from power dissipation in wires and other ohmic heating sources and would have lower local temperatures than typical EP thrusters of half its power.

1.6 The ElectroMagnetic Plasmoid Thruster (EMPT)

For the bulk of this thesis the primary thruster design that was analyzed over the course of several experiments and many different computer models was the ElectroMagnetic Plasmoid Thruster, or EMPT. EMPT is housed at MSNW LLC and funded through NASA Phase I and II Small Business Innovation Research (SBIR) grants. The purpose behind the EMPT program is to develop a 1 kilowatt class electric propulsion thruster with the ability to run on xenon propellant and have an operational lifetime of approximately 15 years. This thruster uses FRC formation and ionization in order to create thrust, unlike traditional Hall thrusters or ion engines which accelerate an unstructured plasma. It is therefore more efficient, as more energy is frozen in the plasma and less is absorbed by the thruster body/other losses. Since the efficiency is high, and the required power is relatively low, this thruster would be ideal for placement on long range NASA science missions. Thus, its primary mission would be for use on interplanetary probes exploring the outer solar system.

FRC thrusters have not had the decades long research and development programs that Hall thrusters have received in the Soviet Union and the USA. As scaling FRC technology to different power levels is still relatively untested, secondary objectives would be for demonstrating the reliability of this subscale FRC based thruster. Currently, there is need for a 50 kilowatt class thruster for use in LEO, MEO, and GEO missions. The Defense Advanced Research Projects Agency (DARPA) is currently pushing for these high power engines for use in propelling Orbital Transfer Vehicles (OTV's). This is because electric propulsion would significantly enhance the reusability of an OTV in servicing military satellites due to an engine specific impulse an order of magnitude higher than the most efficient chemical engines manufactured to date.

EMPT, as it is currently being tested and manufactured, is designed to run at variable power from 1-3 kW. Using xenon propellant, this would correspond to a variable specific impulse of 800-5000 seconds. However, due to the nature of FRC formation, EMPT is not strictly confined to using solely xenon as its primary propellant. An FRC is formed from an ionized gas as detailed previously in Section 1.1, but there is no restriction to what that gas is composed of. EMPT has been run on alternative fuels such as argon, nitrogen, air, ethylene, and vaporized water. This gives it a versatility of use for flexible path and Near Earth Orbit (NEO) style missions. It also enables a possible mission focus on in-situ resource utilization for spacecraft propellant.

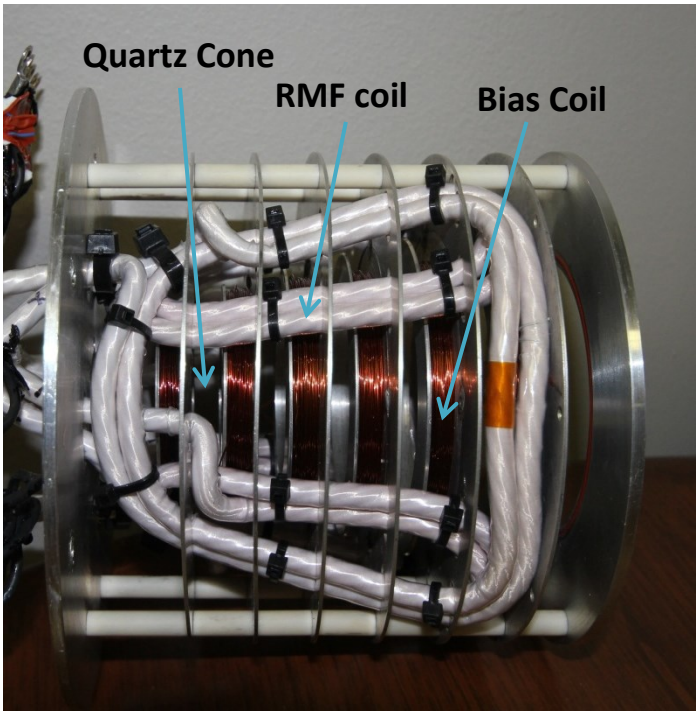

Figure 4. Laboratory model of EMPT Mark III, Version 2

In a laboratory environment, there are several sources of heat that thermal models of EMPT must take into account. First, there is heating of the electronics that drive the RMF coils. The Insulated-Gate Bipolar Transistors (IGBT's) that cause the oscillation of the RMF produce large amounts of waste heat that must be distributed and dissipated in order to prevent overheating and destruction of the

electronics. There is ohmic heating of both the bias coils and the RMF coils from the large amounts of current being produced. In certain EMPT versions, there is coupling between the RMF antennas and other components, which produce additional heat. Lastly, there is radiative heat transfer between the plasmoid and the inner wall of the EMPT quartz cone. Some of these components are listed in Figure 4 for illustrative purposes. The heat produced by these components is distributed throughout the thruster and balances with the heat sinks for the system. In non-vacuum conditions, natural convection from the surrounding air cools the thruster as described by Equation 10. The heat also conducts through whatever material is used to support the thruster during testing and is essentially lost for the purposes of examining the system. Primarily, if the thruster is thermally isolated enough from the supporting structure and in a vacuum, most of the heat will radiate away according to the Stephan-Boltzmann law. However, modeling this is difficult. Radiation is based off of emissivity values which can be estimated, but are difficult to precisely measure due to their dependence on quantities like surface roughness. The same applies for conduction values, as exact values depend on the manufacturing process and impurities in the final product. A table of emissivities and conductivities compiled from various sources is listed in Table 7, Appendix 1. For reasons that have already been detailed, convection is also difficult to estimate. Currently, a vertical wall model for convection is used. That is, a model of still air that becomes less dense with increasing heat and rises, with only cooler air and gravity opposing it. In reality, a detailed fluid simulation would be needed to accurately model the air, taking complex geometry and chaotic (turbulent) fluid motion into account. As these approximations must be made to reduce the complexity of the examined system, some accuracy is lost. However, as will be seen later, the changes in the final temperature values due to these approximations are not significant.

One other difference between experimental setups and theoretical models is thermal contact resistance between parts. In reality, there is an interstitial gap between two objects which is filled with the fluid of the surrounding medium. This is caused by the fact that solid materials do not have perfectly flat surfaces. There are microscopic hills and valleys formed by imperfections in the material or by polishing processes during manufacturing. Thus, two rough surfaces pressed up against each other have a significant gap “resistance” regardless of the conduction values of the surrounding materials. This resistance is heavily based off of the conductivity of the interstitial fluid (air, in most cases). In many instances, the resistance of the gap can be greatly reduced by the use of thermal paste. This thermal paste will generally consist of a non-electrically conductive ceramic that fills the microscopic gaps between materials. This paste is also a much better thermal conductor than air, and so can improve the heat flux across a surface greatly, making it invaluable for cooling purposes.

Chapter 2: Pulsed vs. Steady Approximations

2.1 Introduction

Traditional Electric Propulsion thrusters, as described in Section 1.1, are typically fired continuously after their brief (several hour) startup period. This means that modeling them is relatively simple, as there is a continuous impact of plasma against components and current flowing through the device. FRC thrusters

cannot immediately make this steady assumption, however. Since an FRC is formed from ionizing gas and making a self-contained plasmoid, it is not possible to continuously feed it propellant. Therefore, an FRC device is inherently pulsed and the heat flux it delivers to the wall and the current that drives it are also pulsed. Therefore, it was necessary to analyze the effect of the thruster duty cycle on how much heat is transferred to its different components.

2.2 Pulsed vs. Steady Heat Flux

The thermal solvers in ANSYS® were used to determine how important the pulsed plasmoid formations would be. Two different types of input were used and compared. The first input was a pulsed rectangular wave, representing a pulse of 150,000 W/m^2 heat flux against the quartz thruster cone. This pulse would last for 50 microseconds, followed by a 450 microsecond quiescent period before the next pulse was fired. This input was represented in ANSYS® as a 30th place Taylor Series approximation represented by Equation 17. The MATLAB code for this approximation is shown in Appendix 2, and the output is shown in Figure 5. Tau is the pulse duration in seconds and T is the period in seconds.

Equation 17

$$f(t) = \frac{\tau}{T} + \sum_{n=1}^{\infty} \frac{2}{n\pi} \sin\left(\frac{2\pi n}{T}\right) \cos\left(\frac{2\pi n}{T} t\right)$$

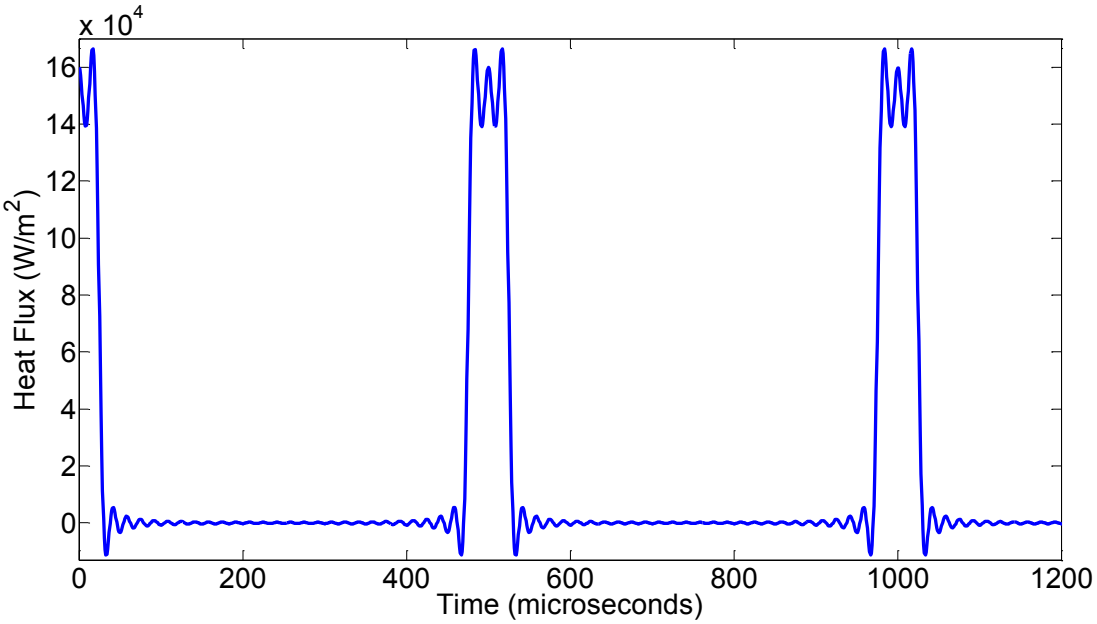

Figure 5. Fourier Series approximation of a pulse train square wave with period of 500 microseconds and pulse duration of 50 microseconds

The thermal solvers available on ANSYS® are capable of handling time dependent inputs to the system, but in order to have the fidelity to capture all of the input, the timesteps taken by the program had to be small. The simulation was run for 15 seconds of simulated time using timesteps of 40 microseconds. This ensured that at least one data point at the peak heat flux would be caught for each pulse in addition to

all of the zeros used during the quiescent period. This was very resource intensive, and required approximately 8 hours to run on a Intel i7 quad core 3.33 GHz CPU.

In an attempt to reduce the amount of time required to perform these calculations, an average of the heat flux was used instead of the pulsed function. This meant that the second type of input used was simply a constant 15000 W/m^2. In comparison, this simulation took only several seconds to solve over the same 15 second simulation time duration as the pulsed version. The results in Figure 6 show that the difference between the two methods is negligible, only 0.01 K, and so averaging the heat flux over the entire duration of the pulse is an acceptable alternative. This allows more complex models to be simulated for longer durations, without needing to use unnecessarily small step sizes which would cause simulations to take days or weeks to converge on an answer.

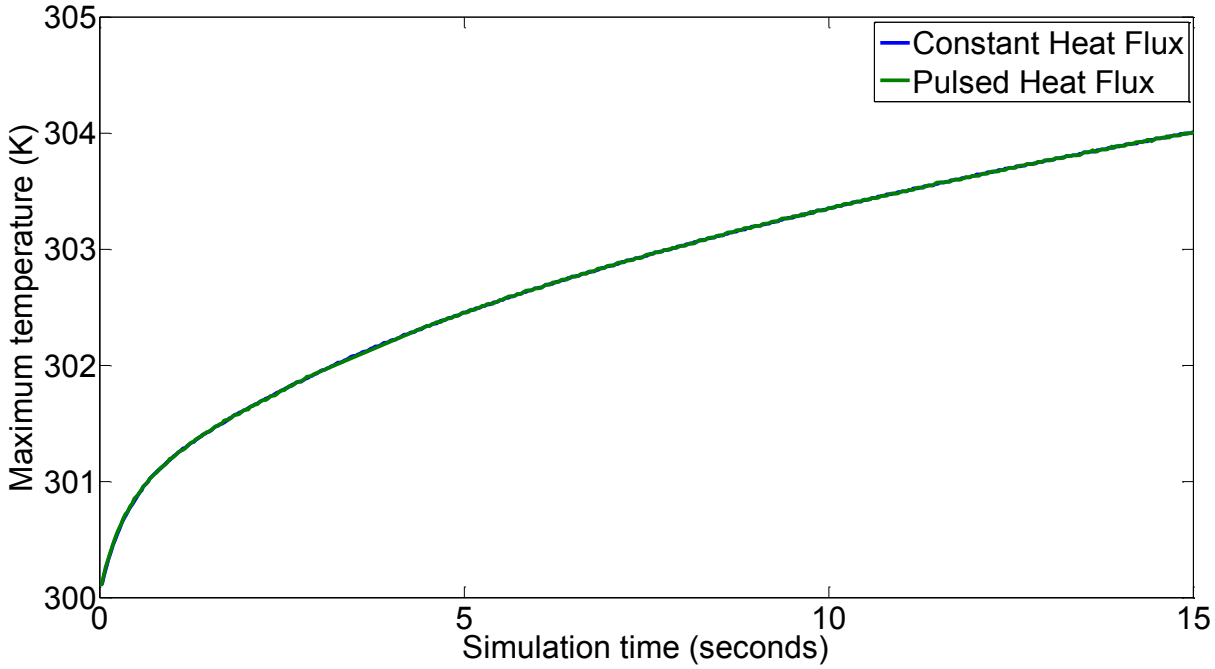

Figure 6. 40 microsecond Pulsed Heat Flux vs. Averaged Steady Heat Flux

Chapter 3: Thruster Model Analysis and Evolution

3.1 Introduction

Starting in 2007, MSNW LLC began to develop the first of several single pulse FRC thrusters. Once characteristics of these single pulse thrusters were sufficiently understood, attempts to create a multi-pulse thruster began. 2010 marked the first time that both multi-pulse and steady state FRC thrusters were assembled and experimented on. The variations of the EMPT Mark III design that have been analyzed with respect to thermal characteristics consist of four computer model versions corresponding to three sequential laboratory models. Later analyses were also run on a completely redesigned

thruster, named the EMPT Mark IV. While experiments and short thermal tests were run on Versions 1 and 2 of EMPT Mark III, the majority of the experimental (validated) results were from Version 3 onwards. Thus, Versions 1 and 2 are discussed only briefly.

3.2 EMPT Mark III, Version 1

As testing continued on the EMPT thruster design, various distinct internal MSNW versions of the thruster emerged. These thrusters were also the first to have extensive thermal tests conducted on the different models. The first model tested is shown in Figure 7. This is the first version of the MARK III EMPT model created in the CAD program Solidworks. Seen at its core, a quartz cone serves as the base support structure and funnels the propellant gas. Attached at the back is an aluminum support plate, which also serves as a heat sink. Macor ceramic rods space six different aluminum disks equally along the quartz cone. This is necessary for bias coils placed in the aluminum flux conservers to shape the axial magnetic field along the cone while maintaining a structure to support the RMF coils. In addition to supporting the RMF coils, these aluminum disks act as large surface areas to radiate heat to the environment. Engineering drawings were produced from this model due to the complexity of the hole pattern used to support this particular RMF configuration. Initial thruster tests determined that the impedance of the plasma load was too low, reducing the circuit efficiency. Therefore, a new design was created to increase the circuit impedance and provide a better model for testing.

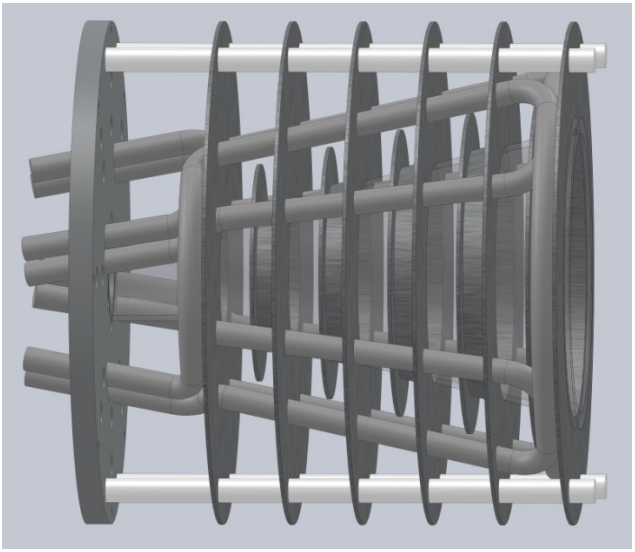

Figure 7. ElectroMagnetic Plasmoid Thruster Mark III, Version 1, with 1 turn RMF coils.

3.3 EMPT Mark III, Version 2

EMPT MARK III, Version 2 rectified previous problems and increased the impedance of the circuit by using a second “turn” on the RMF coil. While this increased the complexity of the thruster and subsequently made assembly more difficult, mutual coupling between the RMF coils and the plasma load was increased, improving the total thruster efficiency. The CAD model of Version 2 is shown in Figure 8. All conductivities and emissivities used were taken from Appendix 1.

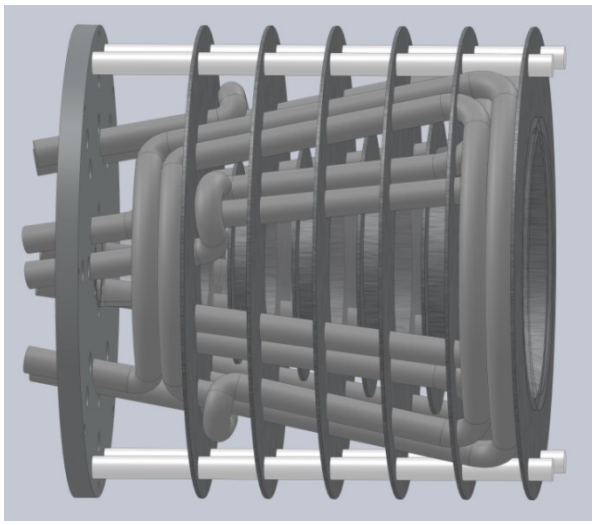

Figure 8. ElectroMagnetic Plasmoid Thruster Mark III, Version 2, with 2 turn RMF coils

Several different methods were used to test this version of EMPT. First, a simple model was set up in ANSYS® using 50 Watts on the inner surface of the quartz cone from plasma radiation. This value was estimated from previous experiments utilizing single pulse FRC's and scaled up to steady state conditions [7]. The model also used a relatively small 2 watts per RMF coil to illustrate internal heat generation from ohmic heating. The purpose of the resulting temperature profile was to determine a baseline reference temperature for EMPT in vacuum conditions. This would give an understanding on how heat would conduct through the different components during initial experimental testing.

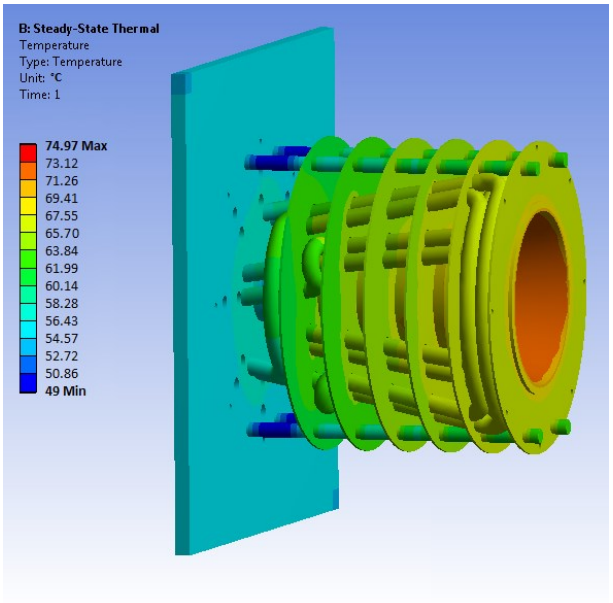

Figure 9. ElectroMagnetic Plasmoid Thruster Mark III, Version 2 with L bracket base, 50 Watts heating to the inner conical surface from plasma radiation and 2 Watts per RMF coil

As is shown in Figure 9, the thrust stand was not modeled at this point in time. To have a better idea of common usage outside the laboratory, the decision was made to model the thruster attached to a "spacecraft." This 1x1m, 1 cm thick aluminum plate "spacecraft" simply served as a heatsink for the thruster while under vacuum conditions. As a result, the simple thruster model was examined under common operating conditions for electric propulsion thrusters attached to spacecraft; that is, with only passive conduction cooling to the spacecraft body and radiation to space. It should be noted, however, that both simulations were performed with an ambient temperature of 22 °C, roughly the same as MSNW vacuum chamber conditions.

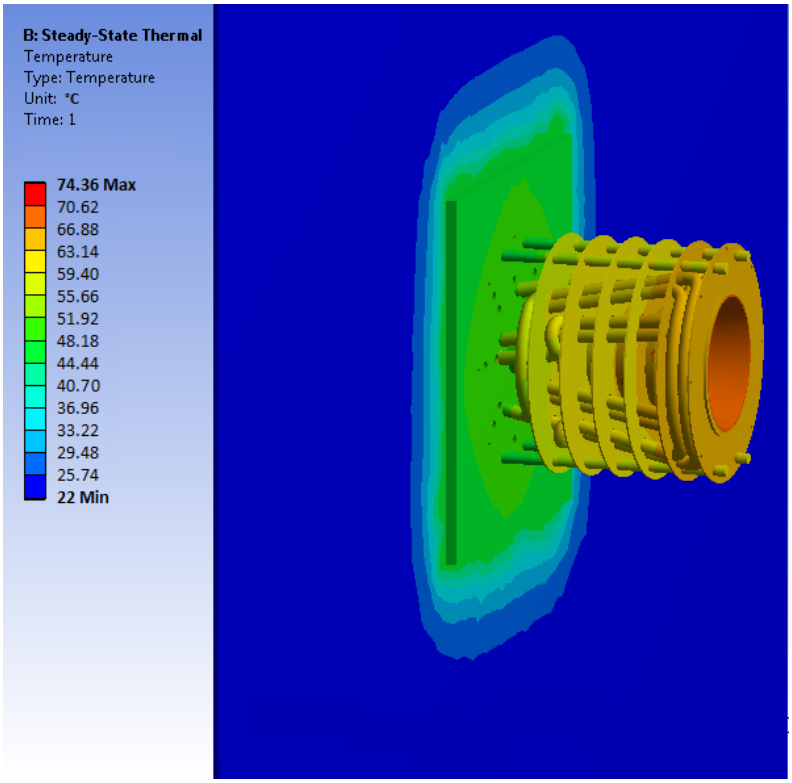

Figure 10. The same thruster as Figure 9 attached to a 1x1 m^2 plate as a room temperature heat sink

3.4 EMPT Mark III, Version 3

Once Version 2 was analyzed, it was determined that the laboratory thruster was at a stage where it could be integrated with the Pulsed Power Unit (PPU) platters that had been already assembled. The resulting thruster with attached footer is shown in Figure 11. A simplified CAD model of the electronics boards was then made to prepare the system for analysis. This model is illustrated in Figure 12. While most of the electronics components on the boards produced heat, the majority of the ohmic heating in the system came from the IGBT switches controlling the high frequency switching current in the RMF coils. Thus, 12 point sources of internal heat generation were used on the primary circular heat sink attached to the footer. Another 12 were placed on the surface of the secondary heat sink located

behind the first. Before thermal analysis on the Mark III could begin, several key thermal characteristics of the thruster had to be determined and the FEM model as a whole validated.

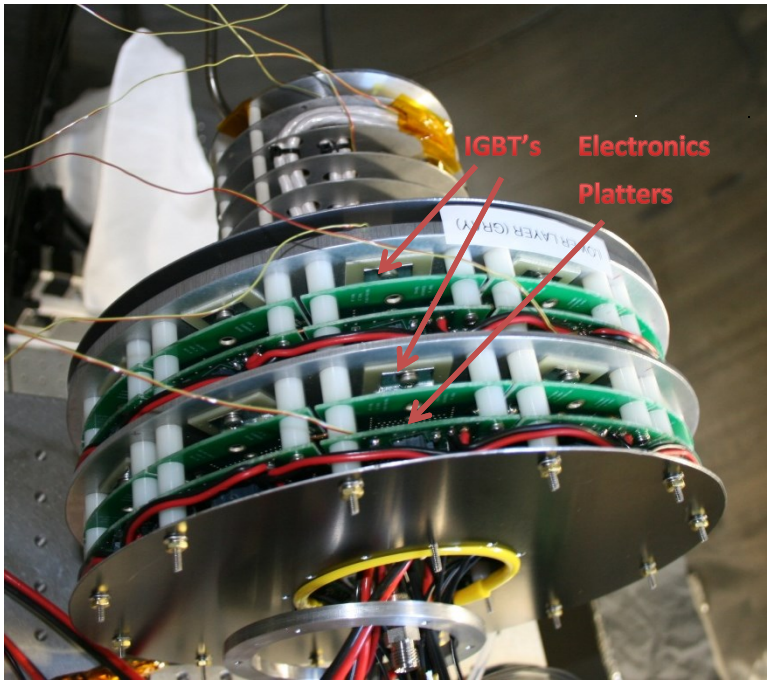

Figure 11. Laboratory model of EMPT Mark III, Version 3 with attached thermocouples inside a vacuum chamber

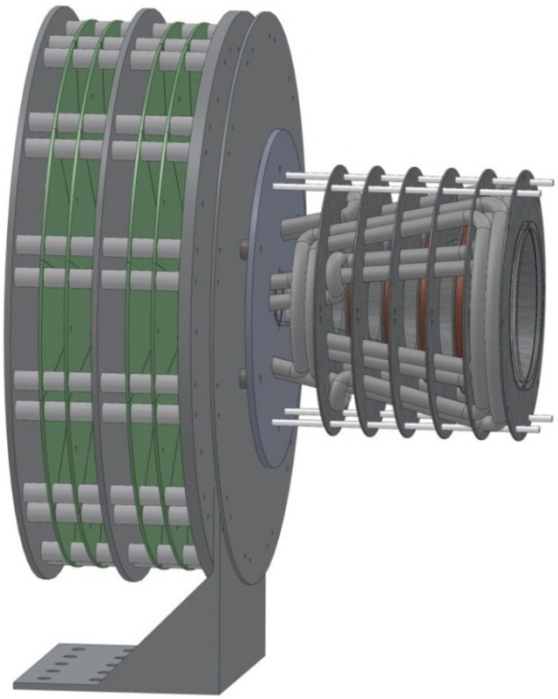

Figure 12. Full EMPT MARK III, Version 3 thruster with attached electronics platters

3.4.1 Electronics Model Validation

During extensive electronics testing of the thruster outside the vacuum chamber, measurements were taken to determine the steady state temperature of different components of EMPT Mark III, version 3. The theoretical temperatures estimated by the ANSYS® model (in vacuum) at different component locations are included in Table 1 for comparison to these experimental values. *Lower* and *Upper* represent each aluminum heatsink with attached IGBTs, one attached to the primary heat sink, and the other to the secondary aluminum sink past the first platters. *Deep Flux* is near the base of the flux conservers and near the base of the thruster cone, while *Near Flux* is toward the end of the cone. *Capacitor* lists the temperature of a capacitor on a PCB board, and *Antenna* lists the RMF temperature next to the Near Flux thermocouple. The units of Table 1 are Δ°C, representing a change in temperature from a base value of 25°C. All temperature values for both analytical computer model and experimental model were taken at $t = 10$ minutes.

Table 1. Change in temperature from a base of 25°C for different thermocouples

	Lower [°C]	Upper [°C]	Deep Flux [°C]	Near Flux [°C]	Capacitor [°C]	Antenna [°C]
Experimental	46	71.3	169.6	126.9	23	109.4
Theoretical	30	42	215	200	15	230

While these two are not directly comparable, these values are off by a margin more significant than would be expected. The primary difference between most experimental data gathered on the real thrusters and the analytical model is simply that the thruster was tested mostly in air, as opposed to vacuum. This means that a major sink of heat was introduced into the model, that of convection. It was determined that the *Near Antenna* and *Deep Flux* thermocouples measured falsely low temperatures in testing conditions due to forced convection from a nearby fan. The *Capacitor*, *Upper*, and *Lower* thermocouples were found to be too high. This was obviously not attributed to the fan and could instead be due to an error in the estimated IGBT power.

In order to validate the results from ANSYS®, extensive testing with an experimental setup needed to be performed to marry the theoretical vacuum models to the experimental air tests. Due to the need to determine both the ohmic heating of the IGBTs and the natural/forced convection cooling of the thruster, a small heat sink plate with attached heat sources was created and modeled. These heat sources consisted of 12 HSA50 resistors, placed to emulate the point source nature of the heat-emitting IGBTs in the actual EMPT electronics. This setup, shown in Figure 13, is isolated from the workbench by a low thermal conductivity block of fiberglass. Six resistors are connected together for each two power supplies.

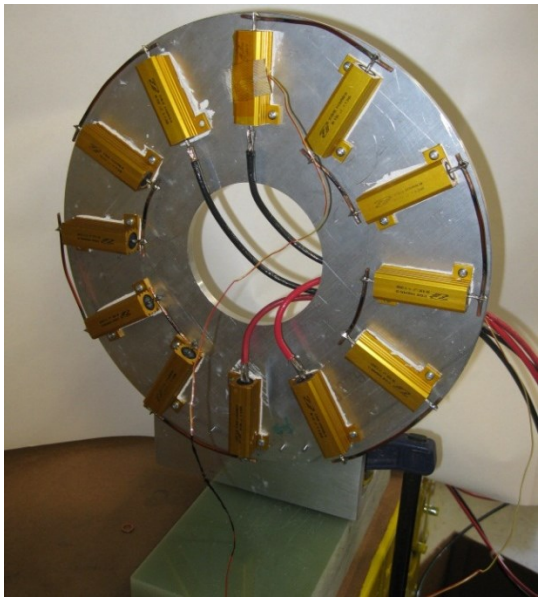

Figure 13. Aluminum heat sink with 12 attached HSA50 0.15 ohm resistors. AOS Heat Sink Compound 300 used to enhance thermal conductivity from resistors to heat sink.

With the addition of a large cardboard box to surround it, the test setup can be effectively prevented from having any forced convection due to ambient air currents in the lab. This means that the only convection acting on the plate and resistors could be estimated by the vertical wall empirical formula in Equation 10. Using a simple MATLAB code detailed in Appendix 2, the convection curve as a function of normalized temperature (T_{plate}-$T_{ambient}$) could be generated for use in ANSYS®. Using the thruster's height as a characteristic length of 0.23 meters and an ambient laboratory temperature of 29°C, the convection curve looked like that in Figure 14. It is again noted that ANSYS® uses a converging algorithm to find the solution to a convection problem, as slightly different temperatures would imply more significant changes in the convection coefficients.

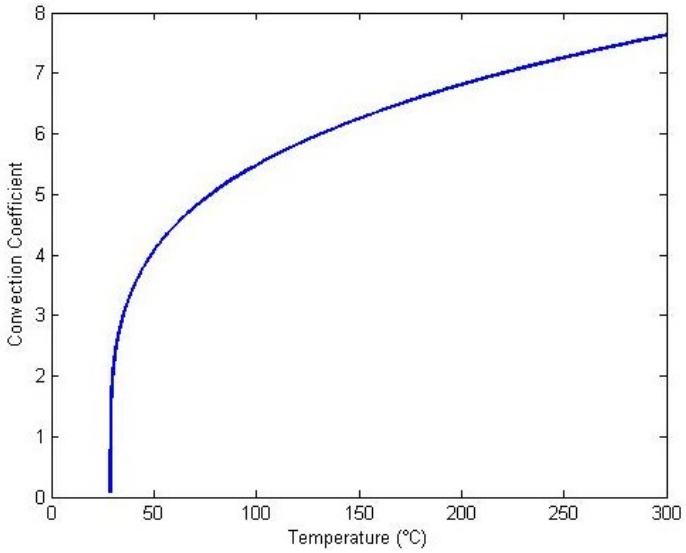

Figure 14. Theoretical convection coefficient vs. plate temperature normalized relative to the ambient temperature of 29°C

Once these values were input into ANSYS®, simulations could be run to validate the choice of different emissivity values for the different components. Using an aluminum emissivity of 0.165, fiberglass at 0.80, and the gold anodized aluminum resistors at 0.82 [8], 134.4 Watts of internal heat generation were divided between all 12 resistors. This emulated the thruster running in real-life testing conditions using a power supply with the resistors in series at 8 volts and 16.8 amps. Running the transient solver in ANSYS® enabled the comparison of time dependent data from the simulation with that of the testing apparatus. The steady state solution, used due to the decreased computational time for iteration, is shown in Figure 15 below. This solution used a fine mesh grid such that a decrease in element sizing only changed the answer by ~0.5°C. This represents a small and fairly negligible error.

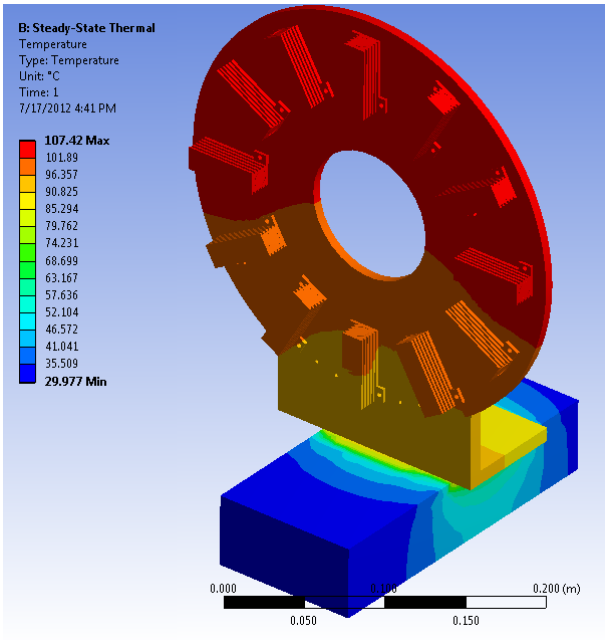

Figure 15. The validation test setup with 134.4 Watts (11.2 Watts/IGBT) running

The highest temperature found in the system, located at the side of the top resistor facing away from the heat sink, was found to be 107.4°C at equilibrium. This was relatively close to the highest temperature recorded in the laboratory of 106.0°C ±3°C at the same midpoint location atop the resistor. However, this does not take into account that the laboratory system was not at full thermal equilibrium. Running the full transient heating simulation for the same 120 minutes as data was taken for the laboratory experiment yielded a maximum temperature of 106.3°C. This is well within the ±3°C error of the thermocouples used. Thus, it was determined that the emissivities mentioned earlier were accurate representations of the laboratory model and that the vertical plane wall convection formula was applicable. The full transient temperature response of the experiment and of the simulation for the top resistor thermocouple is shown in Figure 16 below.

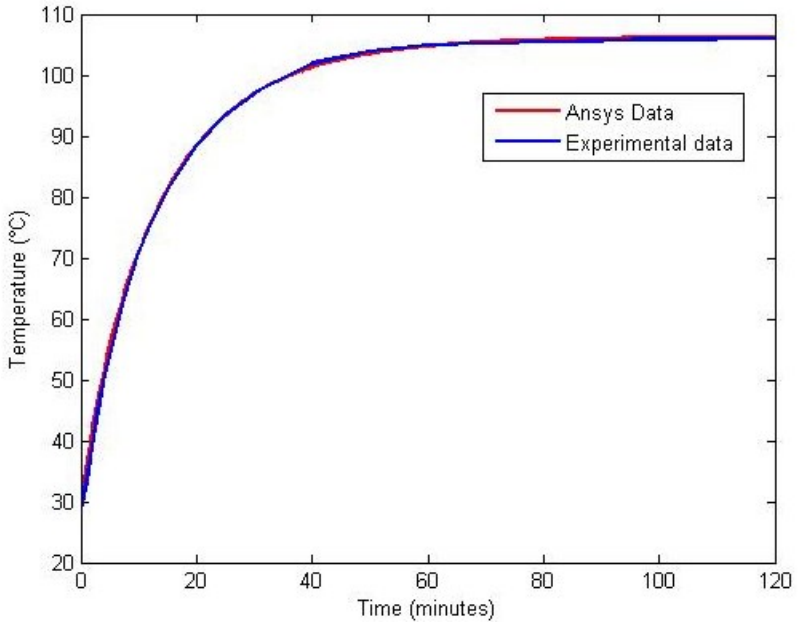

Figure 16. The recorded ANSYS® data and laboratory experimental data using 11.2 Watts/IGBT

The second phase of the electronics validation was to remove the fiberglass base of the setup and replace it with an actively cooled baseplate. This baseplate used local tap water flowing through the base to provide a constant temperature reference for the resistor's heat sink. This modified test setup is shown in Figure 17.

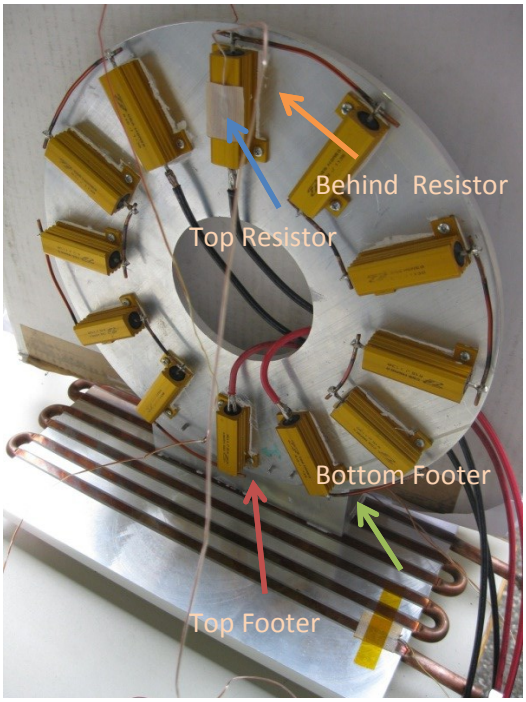

Figure 17. Thermal testing apparatus with cooling baseplate

During the course of electronics testing, Jim Pihl of Raven Technologies took temperature data that could be used as a base comparison to the model in order to determine the power dissipated by the IGBT's. An accurate model of the electronics boards tested in the laboratory was created in Solidworks and imported into ANSYS®. Using the knowledge in regards to emissivity and convection that was acquired through the previous test, a sweep of power levels were run through the IGBT's to determine which best matched up with the experimental results. While the locations of the resistors on the test board were purposefully placed at the same locations as the IGBT's on the actual electronics, there was a size difference between the two, but it would be unimportant compared to the power run through them. Two specific sweep values are presented to illustrate the simulation results. The first sweep consisted of running the two sets of six resistors in parallel. A current of 4.75 amps and a total resistance of 0.9 ohms for each set of six resistors led to a total power per resistor of 3.4 Watts. Comparing the steady state values of different thermocouple locations with the new ANSYS® model resulted in the temperatures below in Table 2. For reference, the ambient temperature was found to be 31°C ±3°C and the water temperature (base temperature) was 19.5°C ±3°C.

Table 2. Comparison of readings from experimental test setup and theoretical ANSYS® values at 3.4 Watts/IGBT

	Theory [°C]	Experimental [°C]
Top Resistor Temp	43.5	42.8
Behind Resistor Temp	43.3	42.5
Top Footer Temp	24.9	27.9
Bottom Footer Temp	19.5	22.7

As can be seen by these values, the difference between the theoretical and experimental is very small-within the ±3°C error of the thermocouples even at the location with the greatest difference. However, it was also necessary to determine if this error would propagate to higher power levels and what effect it would have on the system. Therefore, the second sweep was performed at the same ambient temperature and baseline water temperature, but this time with 9.0 amperes through each pair of 6 resistors. This led to a power per resistor of 12.2 Watts. When this was replicated in ANSYS®, the following readings in Table 3 were acquired.

Table 3. Comparison of readings from experimental test setup and theoretical ANSYS® values at 12.2 Watts/IGBT

	Theory [°C]	Experimental [°C]
Top Resistor Temp	93.5	91.5
Behind Resistor Temp	92.9	91.0
Top Footer Temp	36.5	44.5
Bottom Footer Temp	19.5	26.4

These results show that, while thermocouples reading close to the resistor were still in agreement to within the uncertainty of the probe, the footer values were not. This was attributed to differences between the ANSYS® model and the experimental model, as well as small effects from contact resistance between the different components of the system. However, as both tests found that the top

resistor values agreed with the theoretical values, the final step to finding the power in the IGBT's could be made.

Earlier testing by Jim Pihl had found that the heat sink temperature behind the top IGBT would reach a steady state value of 96°C after two hours, and so an effort was made to match this in ANSYS®. The following simulation results in Figure 18 show that the temperature behind the IGBT would come to 96°C using an input of 12.6 Watts/IGBT. This number is reflected in the EMPT simulations of the previous section.

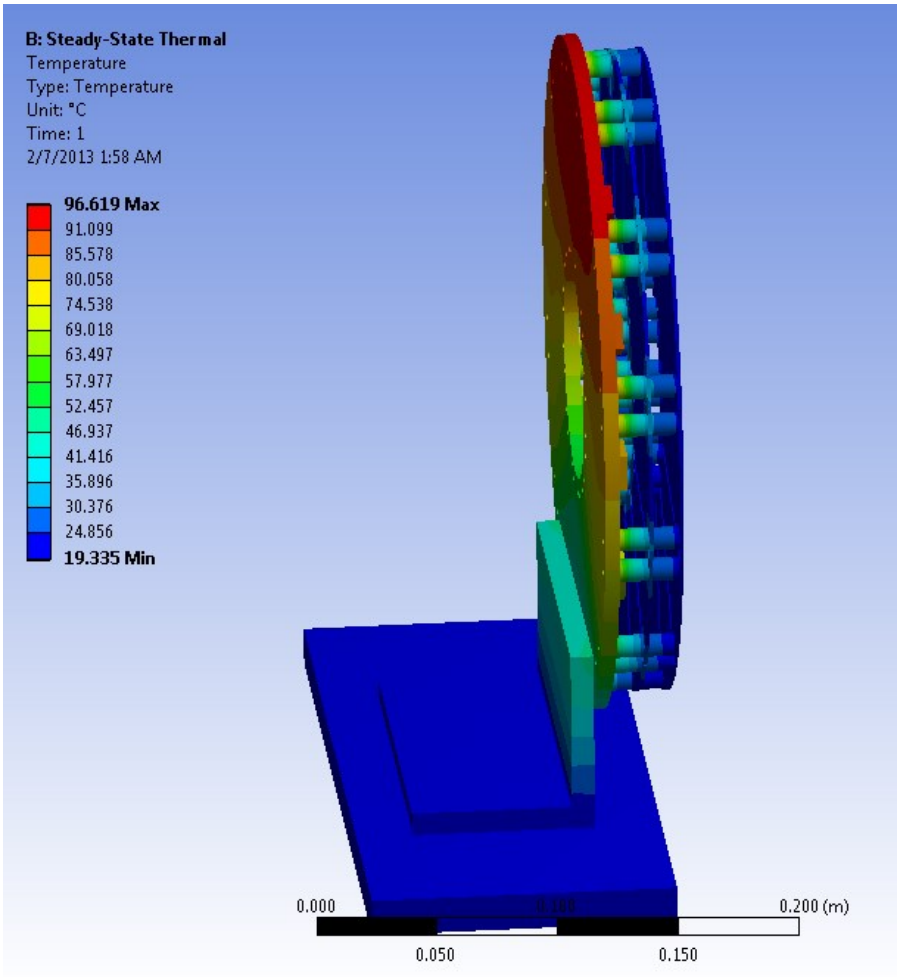

Figure 18. Full model of EMPT electronics as tested by Jim Pihl. Input power of 12.6 Watts/IGBT

Thus, a reliable estimate for the IGBT ohmic heating due to power loss was found and put into the primary EMPT model.

3.4.2 Steady State Thermal Analysis of EMPT Mark III

For the analysis, it was assumed that the thruster would be operating at the ideal total power usage of 1 kW. Different ohmic heat losses and heat generation were estimated from the circuit characteristics of the electronics boards and coupling between the RMF coils and bias coils.

An equivalent circuit resistance for the plasma was determined by comparing a model of the electronic circuit with the electrical response from an experimental FRC pulse and adjusting the model parameters accordingly. For a plasma with a resistance of 0.018 ohms and coupling to the RMF coils, the heating power levels of the various thruster components are shown below in Table 4. It should be noted that the bias coils were omitted due to being small relative to the other power levels. Also, since there was no plasma in the cone, only a proxy load, no heat flux was experienced by the inside of the quartz cone.

Table 4. Power loss for different components in the EMPT thruster for an 0.018 ohm plasma

	Power Loss (Watts)
RMF Coils (Inner)	132.0
RMF Coils (Outer)	132.0
Bias Coils	-
Flux Conservers	60.0
Quartz Cone Absorption	-
Electronics (Per IGBT)	12.6

Similarly, the emissivities of the different components in EMPT also needed to be estimated, in absence of a reliable thermal imaging system to determine them independently. The values used in the following analyses were taken from the sources in Appendix 1. Unlike in previous examinations of the thruster, this time PCB electronics plates, nylon electronics spacers, and various aluminum surface coatings were also considered.

The first simulation of an 0.018 ohm plasma used the basic emissivity values for aluminum on both the heat sinks and flux conservers. The large baseplate was used as the primary conductor of heat for the system. As this simulation took place in vacuum, there was no additional cooling from convection. The only power transfer out of the model came from radiative cooling to the surrounding chamber at 25°C. The model shown in Figure 19 illustrates the primary problem with the EMPT thruster at these power levels – that the maximum temperature reached on the thruster will destroy certain components. Although the quartz cone is capable of withstanding temperatures in excess of 725°C, the Litz wire that the RMF coils are composed of will begin to fail around 200°C. However, the Tefzel® Teflon tubing surrounding the Litz has a maximum operating temperature of 150°C [9]. In addition, the PCB boards and attached IGBT's have reached approximately 205°C, which is far above their maximum temperature of 150°C. These are clearly unacceptable operating temperatures, and so work proceeded on attempts to mitigate them.

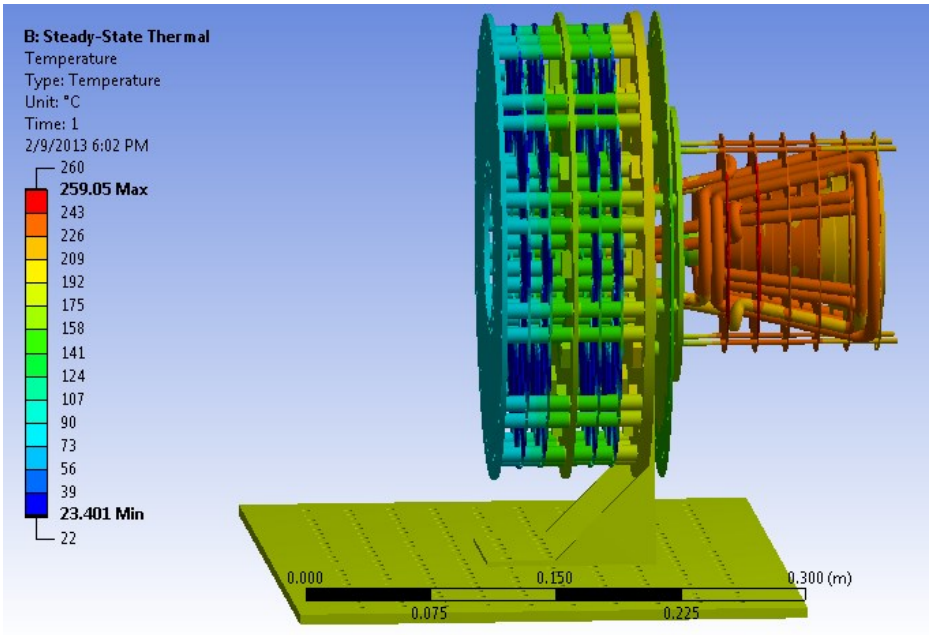

Figure 19. 0.018 ohm plasma, large baseplate, radiatively cooled with 0.105 emissivity value for aluminum

The following simulation in Figure 20 shows an 0.018 ohm plasma with anodized heat sink plates and flux conservers. Using a commercial black anodized surface as a base, the temperatures on the different thruster components were reduced. However, it was found that even though the IGBT's might be within an acceptable temperature range, the heat from the thruster was simply not conducted well enough to the heat sinks to cool the RMF coils to 150°C.

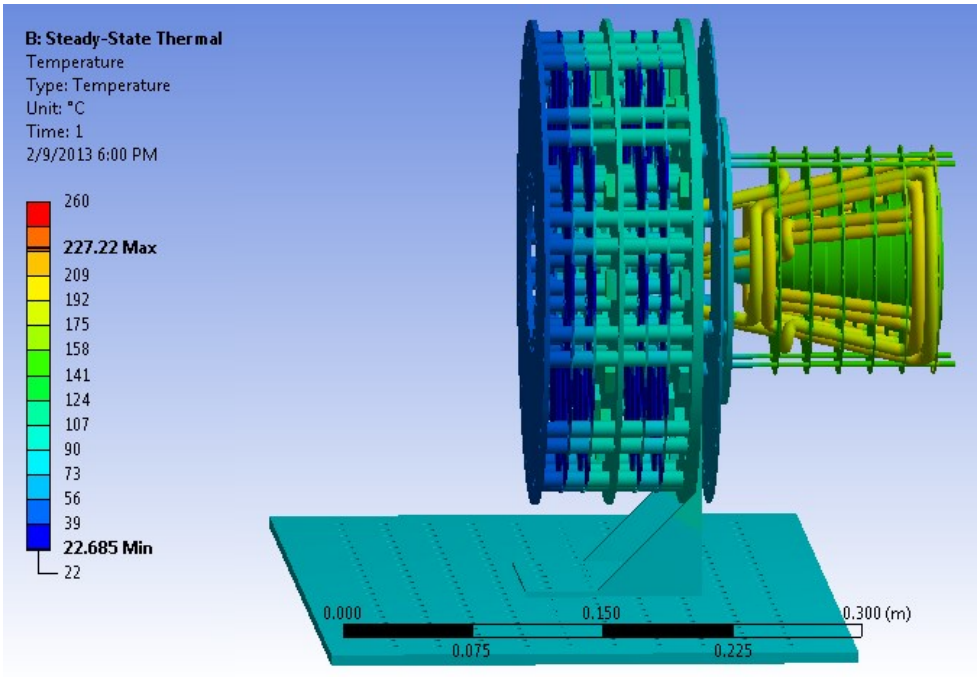

Figure 20. 0.018 ohm plasma, large baseplate, radiatively cooled with 0.900 emissivity value for aluminum

A third simulation was performed in order to determine the efficacy of a water cooled baseplate on the thruster. The primary tapped baseplate was replaced with one set at a constant temperature of 22°C. However, as Figure 21 shows, the conduction through the thruster was again not sufficient to allow the RMF coils to be cooled to a satisfactory temperature.

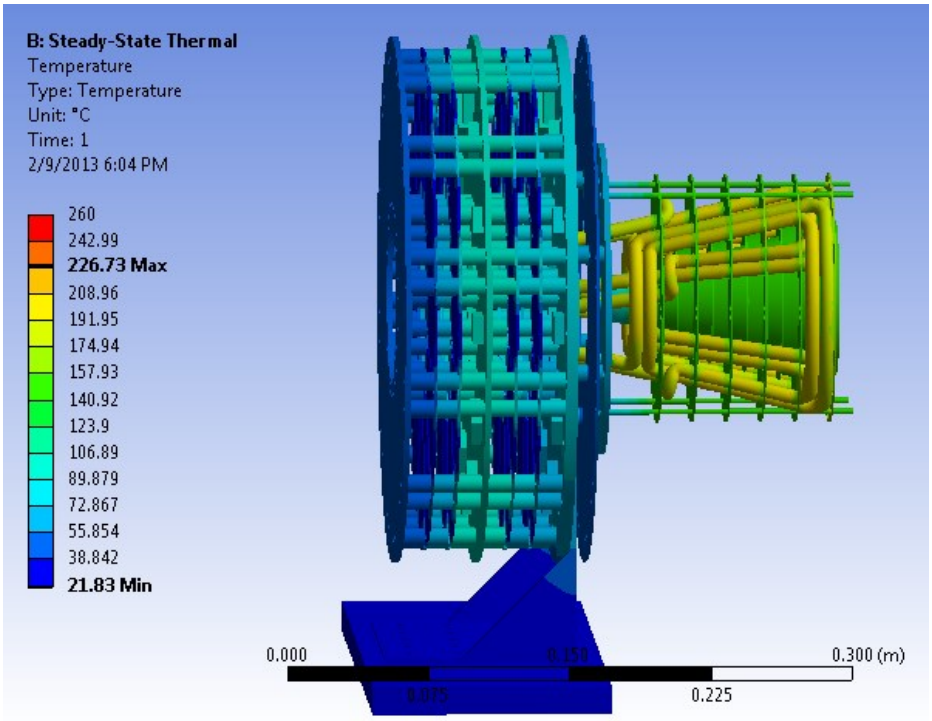

Figure 21. 0.018 ohm plasma, large baseplate, actively cooled (to 22°C) with 0.900 emissivity value for aluminum

The fourth simulation is similar to the first, but with the power levels reduced slightly. A 0.055 ohm plasma load was used with the corresponding power losses described in Table 5. As a higher equivalent circuit resistance represented a more efficient coupling between the RMF coils and the plasma, less energy was dissipated as ohmic heating in the coils.

Table 5. Power loss for different components in the EMPT thruster for an 0.055 ohm plasma

	Power Loss (Watts)
RMF Coils (Inner)	35.7
RMF Coils (Outer)	35.7
Bias Coils	-
Flux Conservers	60.0
Quartz Cone Absorption	-
Electronics (Per IGBT)	12.6

The resulting picture in Figure 22 shows the thruster in steady state with these new power values.

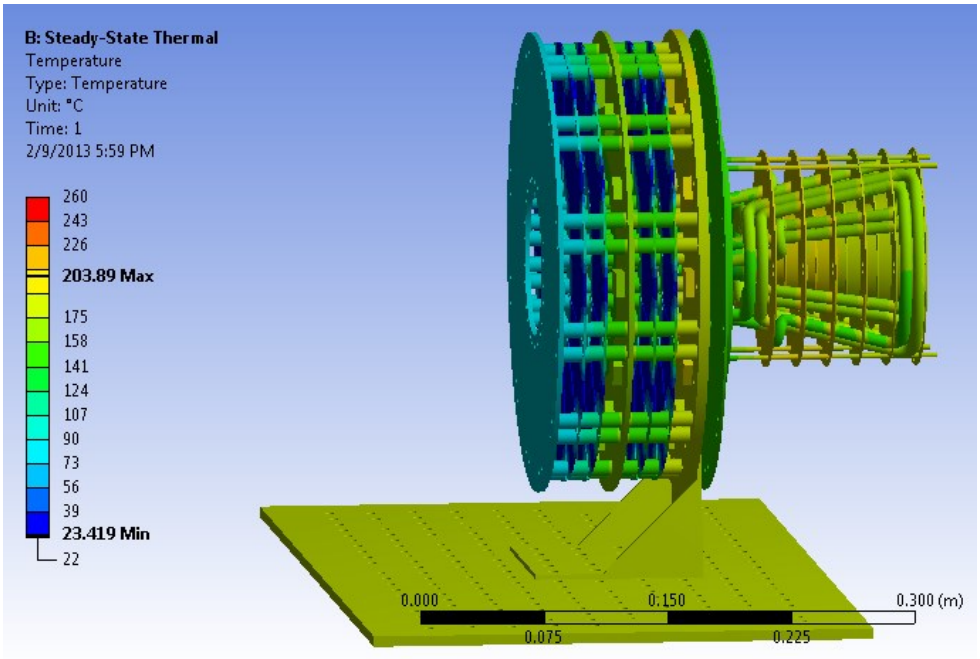

Figure 22. 0.055 ohm plasma, large baseplate, radiatively cooled with 0.105 emissivity value for aluminum

Even with a more conservative estimate for the plasma resistance, it is still obvious that the Litz wire RMF coils are exposed to undesirable temperatures. Due to these models, and to similar experiments conducted in the vacuum chamber with thermocouples, the decision was made to redesign the EMPT thruster in order to prevent failure within the RMF coils.

3.5 EMPT Mark IV, Version 1

In order to prevent failure of the Litz wire, EMPT was redesigned using pure copper RMF coils. This would, unfortunately, only support high frequency current one skin depth into the coil, and so would result in higher resistance. The redesigned thruster with solid copper RMF coils is shown in Figure 23. Due to laboratory testing, it was found that the RMF coils in the previous versions of EMPT tended to couple electrically to the aluminum flux conservers beneath. This was mitigated by moving the flux conservers outside the RMF coils. This also allowed them to be used as simple structural supports, shown by the tabs and Macor supporting rods.

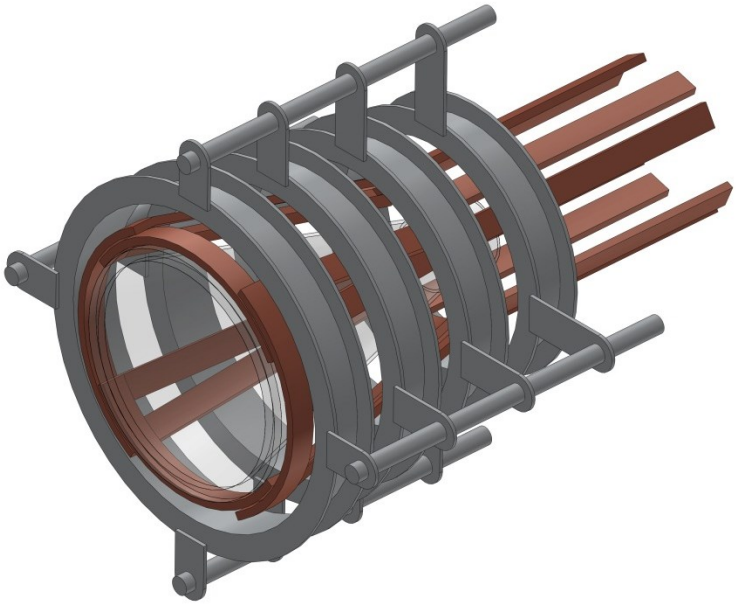

Figure 23. Free floating (unsupported) representation of EMPT Mark IV

The changes made to EMPT did have several advantages that outweighed the increase in weight. First, the copper strips bent into shape for use as coils would retain their shape as a rigid body, unlike the flexible RMF coils used before. This allowed for a far lighter and less complex structural system to hold the RMF coils in place over the thruster cone. Second, since the coils were made out of copper alone, they could easily withstand temperatures past 429°C. Since 429°C represented the most pessimistic view of the thruster heating, this was deemed to be an acceptable alternative.

The Mark IV EMPT thruster was still being manufactured at the end of the ANSYS® analysis, so no simulations are available.

Chapter 4: High Power Pulsed Thruster Modeling

The Electrodeless Lorentz Force (ELF) thruster was being designed concurrently to the next generation of EMPT so a study was run to determine its possible thermal problems at a steady-state power level of 30 kW.

Using previous empirical evidence as a basis for estimating heat losses from each subsystem, a table of heat loads was produced. Using the total input power to the system, different values for the total loss (efficiency) of the system, and the aforementioned heat loss per system, the total power lost by the system in terms of heat goes as below. These values, excluding electronics, were taken from [10]. The electronics power estimations were made from laboratory testing.

Equation 18

$$SystemPower_{lost} = SystemPower_{input} * Efficiency * SubSystemPower_{loss}$$

One assessment was done of a single power level on the existing 1 kW EMPT thruster to compare with experimental ELF data. A sweep at different efficiencies was performed for a prototype of the proposed 30 kW ELF thruster in order to gain an advanced estimate of steady state temperatures at that power level. This sweep included power efficiencies of 1%, 5%, 12%, and 25%. These numbers were used in conjunction with models from Solidworks, and ANSYS®. Table 6 below compares the power sweep for ELF and the comparison assessment for EMPT.

Table 6. Comparison of Power Levels and Estimated Subsystem Efficiencies Used in FEM Analysis of ELF and EMPT Thrusters

ELF Total Power Input (Watts)	Subsystem Power Loss	Efficiency
30000 Watts		System Power Loss [W]
		1%
RMF Coils (Inner)	1.75%	5.3
RMF Coils (Outer)	1.75%	5.3
Bias Coils	3.5%	11
Flux Conservers	7.0%	21
Quartz Cone Absorption	33.3%	100
Electronics	52.6%	158
		5%
RMF Coils (Inner)	1.75%	26.3
RMF Coils (Outer)	1.75%	26.3
Bias Coils	3.5%	53
Flux Conservers	7.0%	105
Quartz Cone Absorption	33.3%	500
Electronics	52.6%	789
		12%
RMF Coils (Inner)	1.75%	63.2
RMF Coils (Outer)	1.75%	63.2
Bias Coils	3.5%	126
Flux Conservers	7.0%	253
Quartz Cone Absorption	33.3%	1200
Electronics	52.6%	1895
		25%
RMF Coils (Inner)	1.75%	131.6
RMF Coils (Outer)	1.75%	131.6
Bias Coils	3.5%	263
Flux Conservers	7.0%	526
Quartz Cone Absorption	33.3%	2500
Electronics	52.6%	3947

EMPT Total Power Input (Watts)	Subsystem Power Loss	Efficiency
1000 Watts		System Power Loss [W]
		12%
RMF Coils (Inner)	1.75%	2.1
RMF Coils (Outer)	1.75%	2.1
Bias Coils	3.5%	4.2
Flux Conservers	7.0%	8.4
Quartz Cone Absorption	33.3%	40.0
Electronics	52.6%	63.2

It should be noted that the subsystem power losses are estimates, reflected in the fact that a sweep was done up to a 25% power lost to heat from the thruster, which is a far greater loss than the thruster will actually experience, and so represents the 'worst case' scenario. Due to these estimates, the FEM analyses run on the 30kW thruster are not as accurate as the EMPT thruster. Because of the accuracy of the EMPT model compared to the laboratory built thruster, the heat flow between parts could be modeled with a much higher fidelity and results could be immediately compared to experimental results. As mentioned previously, knowledge gained from the EMPT analysis could then translate into accuracy improvements for estimations of heating at higher powers. The first design of the 30 kW ELF thruster is shown in Figure 24. This design used only non-anodized 6061 aluminum (dull emissivity), copper, and quartz. Thus, it is designed to withstand high temperatures.

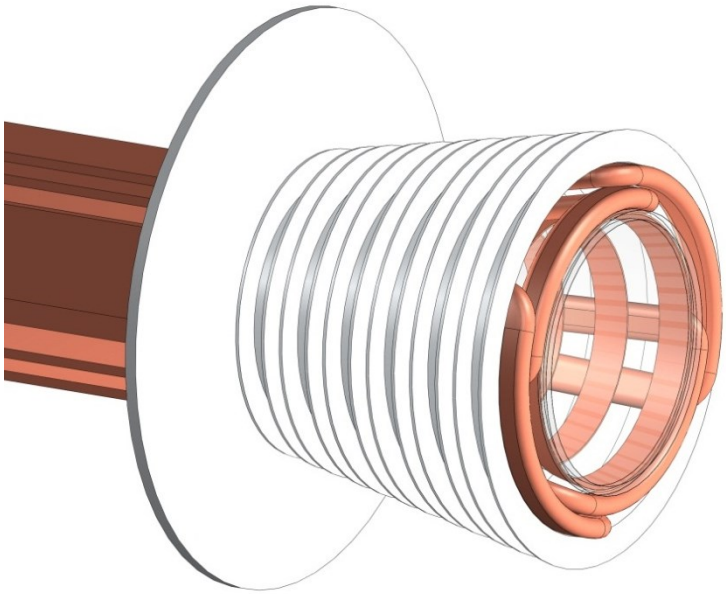

Figure 24. CAD model of 30kW ELF

For the most part, the primary focus of these simulations were on the end of the electrical feed system, a strip of copper 1/8" thick leading to the copper RMF coils. Due to the energy output of the system, and subsequent ohmic heating, the electronics powering the RMF coils would become extremely hot. The following figures serve to illustrate the difficulty in keeping the PPU section of the thruster cool, even for increasing lengths of stripline up to 1 meter. For reference and for the sake of brevity, the 12% loss values are the only ones presented below. These first simulations do not include the electronics heating, which will be included later. For the following tests, vacuum chamber conditions were set for each thruster variation. This means that, while the components still conducted to each other, they only lost heat through radiation, rather than convection.

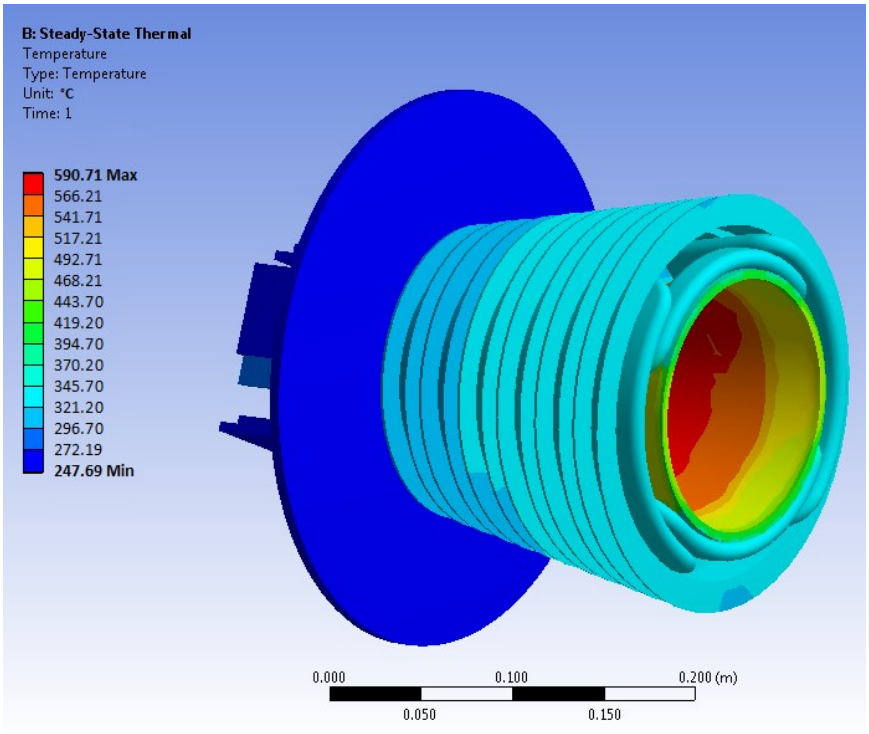

Figure 25. 30 kW ELF thruster with 0.1 m stripline at 12% heating, no PPU heating

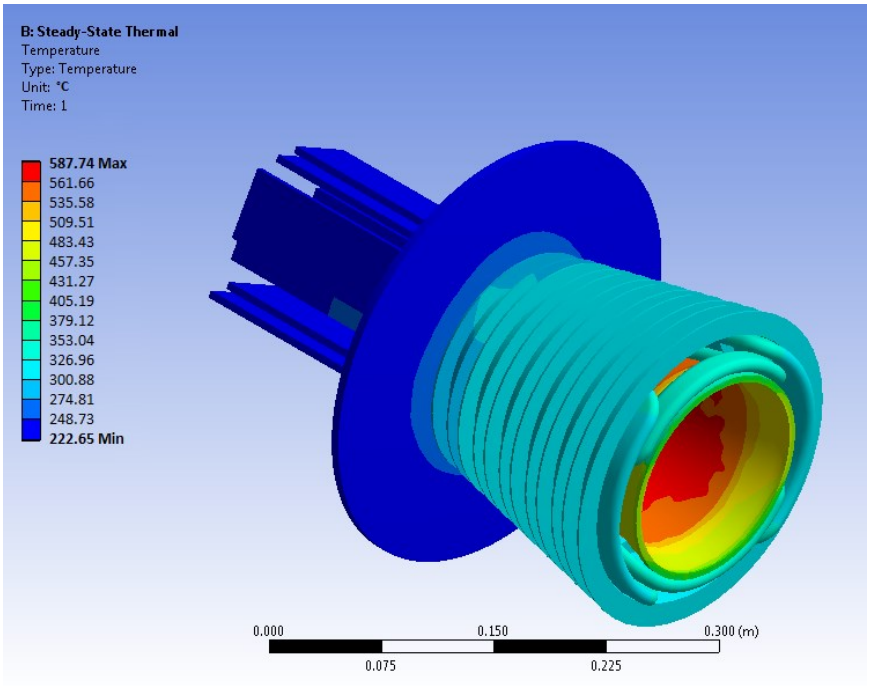

Figure 26. 30 kW ELF thruster with 0.2 m stripline at 12% heating, no PPU heating

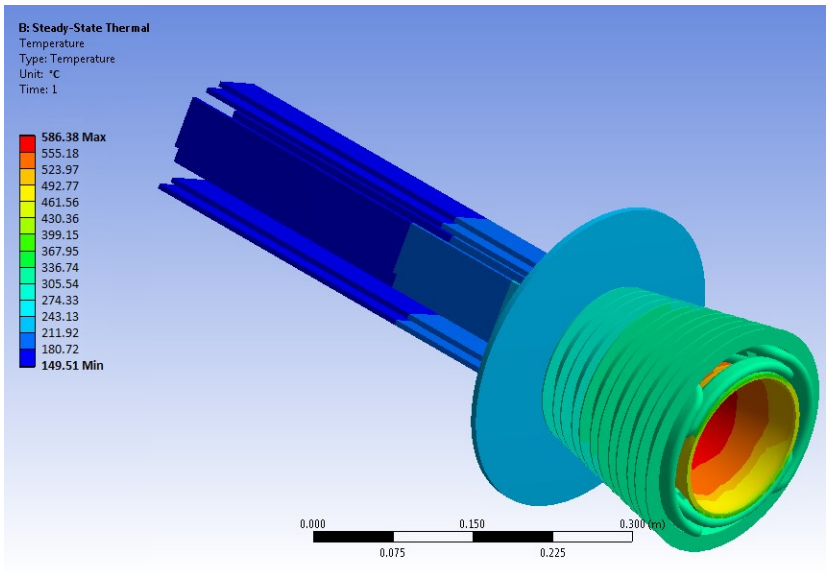

Figure 27. 30 kW ELF thruster with 0.5 m stripline at 12% heating, no PPU heating

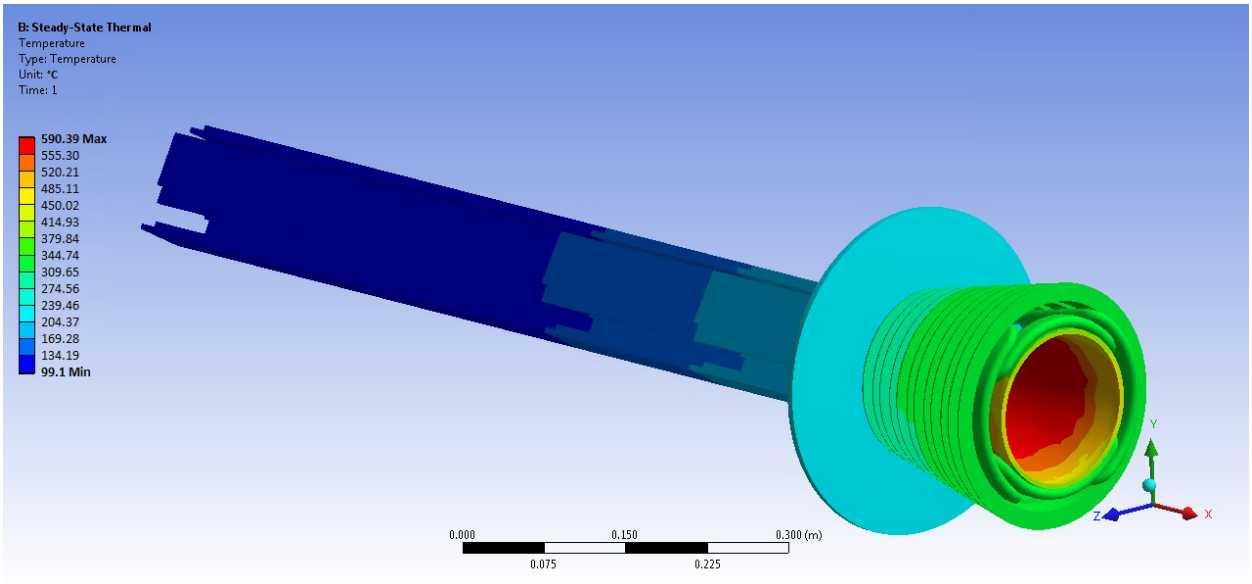

Figure 28. 30 kW ELF thruster with 1.0 m stripline at 12% heating, no PPU heating

As would be expected, the end of the stripline's temperature radically decreases as the length increases. Across all power loss levels, this trend remains true, as shown in Figure 29. Note that the ambient temperature of the surroundings for all simulations was set to be 22°C.

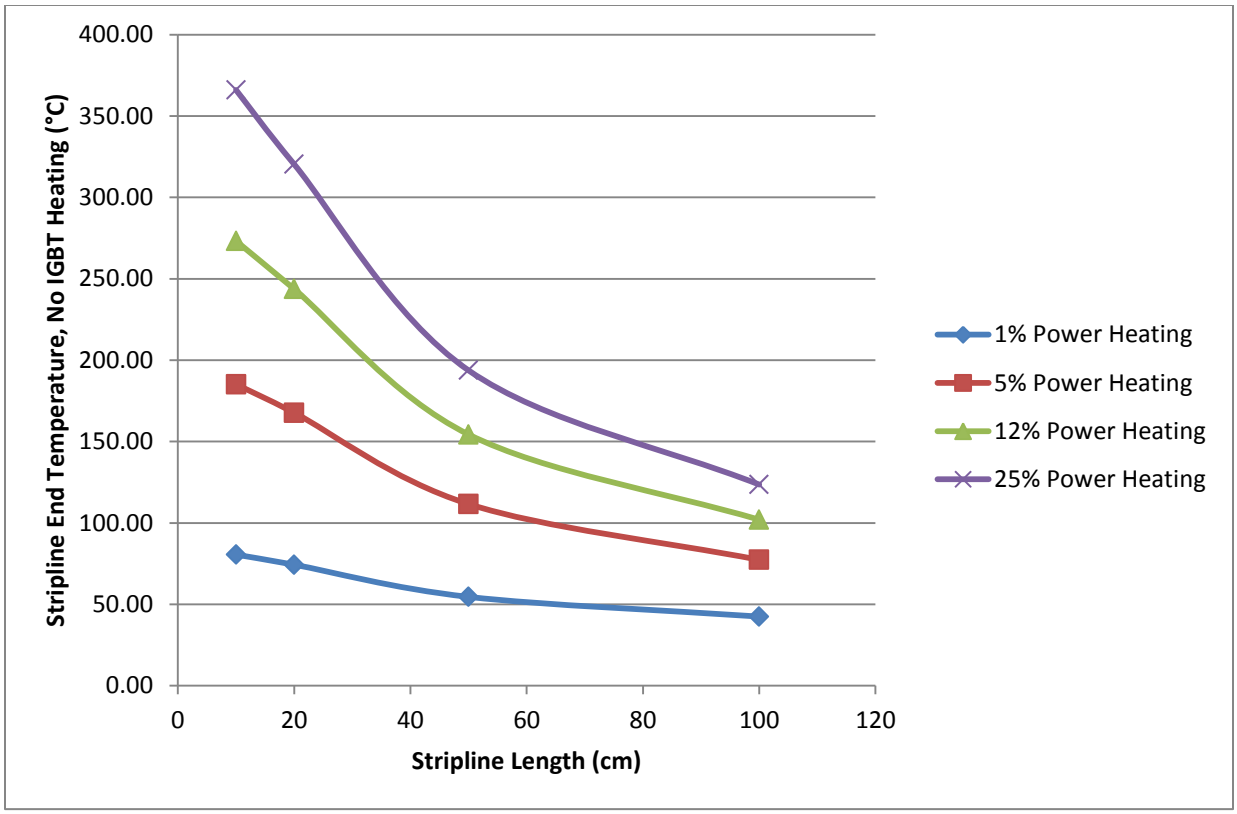

Figure 29. ELF ANSYS® Results, steady state, no heat sinking, no electronics heating

The full data for all recorded locations of interest for all power loss levels is available in Appendix 1. While all of the temperatures recorded on the stripline were within acceptable limits, the 25% loss values could arguably be within the annealing temperature range for copper (1/2 of melting temperature, or ~405°C), which would change the physical properties of the material. In order to mitigate this kind of behavior, the data shows that a simple increase of the stripline length of 10 cm could decrease the stripline end temperature by 50°C at the hottest power level. However, it should also be noted that the RMF coils inside the aluminum flux conservers reached 475°C for the 25% loss case, which is above the annealing temperature. For practical engineering applications, the type of copper used in the thruster manufacturing process would have to be chosen carefully, in absence of any active cooling mechanisms.

Overall, the data from the simulation sweeps including the electronics heating risks the possibility of structural failure. However, this is a fairly pessimistic view of the thruster's thermal characteristics. By mitigating the power transferred from the PPU into the striplines with an active cooling system, the results without electronics show that the thruster could operate well within nominal temperature ranges, even up to the highest power loss levels. Thus, future solutions will have to be devised to actively cool the driving electronics for the thruster.

Chapter 5: Future Work

Currently, there are several projects ongoing at the MSNW facilities that could benefit from thermal analysis. The EMPT Mark IV, Version 1, could easily be matched with the simulations already run of the IGBT's, and preliminary results could be compared to experimental data. In order to do so, the convection models developed in this paper would also need to be used. Comparisons like these would allow for further refinement of the ANSYS® thermal model for FRC thrusters. Further into the future, work would need to begin on the analysis and thermal implications of a 100 kW FRC thruster.

5.1 Estimations and Comparisons

The largest estimation in these thermal analyses is that of the heating from the plasma itself and the power losses from RMF coupling to the flux conservers. While steady state testing has gone forward with the EMPT laboratory models, long duration tests with attached thermocouples would be needed in order to determine the precise nature of the heating factors involved. It is currently unknown how the different wavelengths of electromagnetic radiation would interact with the thruster body. While the optical properties of the quartz are known, the plasma's are not. Careful examination of the FRC would have to be made to determine the impact of reflectivity and transmittivity as a function of wavelength on the quartz. This would also change based off of the propellant gas type. As the FRC based thruster is designed to function on any gaseous, ionizable propellant, tests would have to be run on each different gas to be commonly used.

Another feature not accounted for in the current ANSYS® models is the changing of resistance based off temperature. Especially for the 30 kW thruster, temperature rises of 400°C would consequently cause extremely large rises in circuit resistance, dramatically changing circuit efficiencies. Future models would need to use an iterative scheme either manually or by a script within ANSYS® to account for these changes.

Chapter 6: Conclusion

This paper has served to show the current state of the FRC based thrusters EMPT and ELF at the MSNW LLC laboratories. The lower power 1 kW EMPT, having gone through three iterations and one major redesign, is now far more capable of withstanding the temperatures it will encounter in vacuum conditions. The IGBT heating power levels, having been proven to within a reasonable degree of certainty, can now be used to help validate future models. In conjunction with the convection model, comparison with thermocouple data during standard experiments should be relatively simple. The higher power 30 kW ELF model has been shown to consistently reach acceptable temperatures regardless of power load assuming active cooling of the PPU. Active steps will have to be taken to thermally isolate the electronics from the rest of the thruster and apply the same level of thermal design rigor as has been implemented on the EMPT with the help of this thermal modeling effort.

Bibliography

[1] F. P. Incropera, D. P. Dewitt, T. L. Bergman and A. D. Lavine, Fundementals of Heat and Mass Transfer, Hoboken: John Wiley & Sons, 2007.

[2] SAS IP, Inc., "ANSYS 13.0 Help," ANSYS Inc., 2010.

[3] J. R. Welty, C. E. Wicks and R. E. Wilson, Fundementals of Momentum, Heat, and Mass Transfer, Corvallis: John Wiley & Sons Inc., 1984.

[4] NASA, "TacSat-2," 2006. [Online]. Available: http://www.nasa.gov/mission_pages/tacsat-2/main/index.html. [Accessed 14 September 2012].

[5] T. S. Matlock, W. A. Hargus and C. Larson, "Thermographic Characterization and Comparison of 200W and 600W Hall Thruster," in *43rd Joint Propulsion Conference*, Cincinnati, 2007.

[6] J. L. Van Noord, "NEXT Ion Thruster Thermal Model," in *43rd Joint Propulsion Conference*, Cincinnati, 2007.

[7] T. E. Weber, The Electrodeless Lorentz Force Thruster Experiment, Seattle: University of Washington, 2010.

[8] Electro Optical, "Material Emissivity Properties," 2000. [Online]. Available: http://snap.fnal.gov/crshield/crs-mech/emissivity-eoi.html.

[9] Dupont, "Tefzel® ETFE Resin Chemical Use Temperature Guide," 2013. [Online]. Available: http://origin.dupont.com/Teflon_Industrial/en_US/assets/downloads/h96532.pdf. [Accessed 6 March 2013].

[10] J. Slough and D. Kirtley, "Pulsed Plasmoid Propulsion: The ELF Thruster," in *31st International Electric Propulsion Conference*, Ann Arbor, 2009.

[11] P. Auerkari, "Mechanical and Physical Properties of Engineering Alumina Ceramics," Technical Research Centre of Finland, Espoo, 1996.

[12] Monarch Instruments, "Table of Total Emissivity," [Online]. Available: www.monarchserver.com/TableofEmissivity.pdf.

[13] European Cooperation for Space Standardization, "Space Product Assurance: Black-anodizing of Metals with Inorganic Dyes," ESA-ESTEC, Noordwijk, 2008.

[14] T. Ogden, "Thermal Conductivity of Hard Anodized Coatings on Aluminum," Naval Ocean Systems Center, San Diego, 1987.

[15] Williamson, "Aluminum Processing, Noncontact Temperature Measurement," [Online]. Available: http://www.heitronics.com/fileadmin/content/Williamson_Docu/williamson_aluminum_brochure.pdf.

[16] Collaboration for NDT Education, "Conductivity and Resistivity Values for Copper & Alloys," [Online]. Available: http://www.ndt-ed.org/GeneralResources/MaterialProperties/ET/Conductivity_Copper.pdf.

[17] HEBO Spezialglas, "Datasheet, FSUV1 (Fused Silica), FQVIS2 (Fused Quartz)," [Online]. Available: http://www.hebo-glass.com/public/pdf/datasheet_quartz.pdf.

[18] Technical Products, Inc, "G-10 & G-11 (Garolite) Material Specs," 2012. [Online]. Available: http://www.technicalproductsinc.com/garolite_specs.html.

[19] G. M. Carlomagno and G. Cardone, "Infared Thermography for Convective Heat Transfer Measurements," *Experiments in Fluids,* vol. 49, 2010.

[20] H. F. Dawson and M. di Marzo, "Multi-Droplet Evaporative Cooling: Experimental Results," *AIChE Symposium Series, Heat Transfer,* vol. 89, no. 295, pp. 122-131, 1993.

[21] J. M. Curtis, "Experimental Verification for Microwave Processing in a Single Mode Rectangular Resonant Cavity," Virginia Polytechnic Institute and State University, Blacksburg, 1999.

[22] PAR Group, "Nylon 66," PAR Group LTD, Manchester.

[23] M. Honner and P. Litos, "Thermographic analysis of the hot-air soldering of the electronic circuit board," University of West Bohemia, Pilsen.

[24] The Bergquist Company, "Sil-Pad 2000," The Bergquist Company, Chanhasssen.

[25] LESO-PB/EPFL, Enecolo AG, Ernst Schweizer AG, "New Generation of Hybrid Solar PV/T Collectors," Bundesamt fur Energie, 2000.

[26] DuPont, "Dupont Tefzel Properties Handbook," Dupont.

[27] NASA, "DAWN: A Journey to the Beginning of the Solar System," 2007. [Online]. Available: http://dawn.jpl.nasa.gov/. [Accessed 14 September 2012].

[28] Cotronics Corp., "Electrically Resistant Adhesives," [Online]. Available: www.cotronics.com.

Appendix 1

Table 7. Table of different characteristics for commonly used materials

Material	Emissivity	Thermal Conductivity (W/m-K)	Electrical Conductivity (ohm-cm)	Maximum Temperature (°C)
Alumina [11] [12]	0.900	35.00	1.00E+15	1500
Aluminum (Anodized) [13] [14]	0.900	0.70	1.00E+12	100
Aluminum (Dull) [12] [15]	0.105	180.00	3.66E-06	582
Aluminum (Shiny) [12] [15]	0.069	180.00	3.66E-06	582
Copper [12] [16]	0.830	400.00	1.72E-08	1010
Fused Quartz [12] [17]	0.750	1.40	7.00E+07	1683
G-10 Fiberglass [18]		0.29	4.27E+15	140
Macor [19] [20]	0.940	1.46	1.00E+16	800
Nylon [21] [22]	0.730	0.23	1.00E+15	100
PCB (Circuit Board) [23]	0.800			273
Sil-Pad 2000 [24]		3.50	1.00E+09	392
Tefzel [25] [26]	0.950	0.24	1.00E+17	255

Table 8. Standard Copper ELF V2 (Not heat sunk, no IGBT heating) @ Steady State

	1 % Heat Loss				5 % Heat Loss			
	Stripline Length (cm)				Stripline Length (cm)			
Location	**10**	**20**	**50**	**100**	**10**	**20**	**50**	**100**
Backplate	355.41	351.07	341.76	340.85	465.58	456.23	437.70	438.17
Bias 1 (By Backplate)	358.71	355.06	347.51	347.05	479.47	472.91	460.32	461.76
Bias 2	359.72	356.18	348.93	348.57	483.59	477.47	465.85	467.55
Bias 3	360.64	357.18	350.20	349.89	486.88	481.01	470.18	472.05
Bias 4	361.51	358.08	351.41	351.17	489.57	483.76	473.72	475.74
Bias 5	362.31	358.87	352.52	352.34	491.19	485.57	476.31	478.43
Bias 6 (By Plasma)	363.12	359.60	353.54	353.37	493.01	487.10	478.41	480.55
Cone Inside	459.77	456.46	448.26	447.60	682.69	680.70	677.04	677.92
Cone Outside	457.79	454.67	446.49	446.68	673.35	671.30	667.09	664.54
Conservers	457.71	454.58	445.63	445.66	672.66	670.87	666.32	664.55
RMF 1	365.06	361.95	355.68	355.25	499.27	495.33	484.54	485.74
RMF 2	364.01	360.87	354.44	353.93	496.17	491.56	481.28	482.45
Stripline End (IGBT's)	353.70	347.50	327.76	315.66	458.33	440.86	384.77	350.50

	12 % Heat Loss				25 % Heat Loss			
	Stripline Length (cm)				Stripline Length (cm)			
Location	**10**	**20**	**50**	**100**	**10**	**20**	**50**	**100**
Backplate	561.68	549.41	526.94	529.25	667.20	652.79	627.92	631.79
Bias 1 (By Backplate)	586.49	579.16	566.10	569.10	703.10	695.83	683.12	686.97
Bias 2	594.16	587.58	576.01	579.31	714.97	708.71	697.77	701.84
Bias 3	600.08	593.85	583.29	586.80	724.72	718.79	709.02	713.70
Bias 4	604.89	598.58	588.92	593.18	730.88	724.51	715.95	721.84
Bias 5	605.87	599.71	591.68	595.54	730.16	723.70	717.37	722.39
Bias 6 (By Plasma)	607.55	601.14	593.96	597.94	730.62	723.86	718.04	723.24
Cone Inside	863.86	860.89	859.53	863.54	1066.8	1056.9	1057.1	1064.0
Cone Outside	840.44	838.83	838.66	834.38	1014.0	1012.3	1015.8	1011.9
Conservers	838.31	837.49	835.69	830.99	1009.8	1009.6	1009.7	1002.7
RMF 1	623.13	618.60	604.87	608.91	763.97	760.31	745.39	751.85
RMF 2	613.55	609.79	599.50	602.31	740.08	737.75	727.61	731.56
Stripline End (IGBT's)	546.36	516.85	427.51	375.16	639.11	593.48	466.87	396.74

Table 9. Standard Copper ELF V2 (Not heat sunk, IGBT heating) @ Steady State

	1 % Heat Loss				5 % Heat Loss			
	Stripline Length (cm)				Stripline Length (cm)			
Location	**10**	**20**	**50**	**100**	**10**	**20**	**50**	**100**
Backplate	414.10	401.49	372.37	358.66	597.77	559.56	489.64	462.98
Bias 1 (By Backplate)	403.51	393.92	371.49	361.15	561.79	538.27	493.91	477.88
Bias 2	402.00	392.95	371.83	362.07	556.82	535.83	496.32	482.21
Bias 3	403.45	394.25	372.57	362.99	560.11	538.80	498.60	485.69
Bias 4	402.04	393.38	373.03	363.94	554.94	536.02	500.25	488.57
Bias 5	401.27	393.03	373.81	364.92	551.60	534.34	501.84	490.83
Bias 6 (By Plasma)	401.60	393.55	374.74	365.92	551.42	535.15	503.69	492.89
Cone Inside	481.48	475.73	460.76	454.36	716.45	704.08	688.23	682.73
Cone Outside	479.48	473.75	458.46	453.57	705.04	694.22	678.82	669.06
Conservers	479.44	473.75	458.26	452.34	703.84	694.20	677.82	669.07
RMF 1	416.32	403.97	377.63	367.80	606.59	568.96	513.15	498.30
RMF 2	414.67	401.78	375.78	366.54	600.70	561.06	507.14	495.03
Stripline End (IGBT's)	433.71	433.63	418.42	423.59	687.12	694.14	663.18	687.68

	12 % Heat Loss				25 % Heat Loss			
	Stripline Length (cm)				Stripline Length (cm)			
Location	**10**	**20**	**50**	**100**	**10**	**20**	**50**	**100**
Backplate	748.15	681.02	581.71	551.79	901.12	800.99	679.27	650.52
Bias 1 (By Backplate)	687.16	651.16	596.29	581.57	815.03	767.39	707.71	696.17
Bias 2	679.21	648.52	601.96	590.07	804.90	765.97	717.77	709.40
Bias 3	683.48	652.48	606.95	596.48	810.06	770.78	726.61	720.40
Bias 4	674.50	648.35	609.78	601.83	797.29	765.67	730.34	727.39
Bias 5	668.17	645.28	610.88	603.62	787.51	760.88	729.49	727.11
Bias 6 (By Plasma)	666.46	645.60	612.84	605.92	783.08	759.74	730.26	728.05
Cone Inside	908.76	884.29	868.41	866.76	1113.9	1079.9	1064.0	1066.6
Cone Outside	879.88	862.49	848.01	838.46	1060.7	1038.6	1023.3	1015.0
Conservers	878.87	861.71	844.86	834.82	1056.6	1033.6	1016.9	1005.6
RMF 1	764.46	701.90	632.30	619.91	926.52	841.03	767.41	759.85
RMF 2	754.79	682.68	619.06	610.56	911.81	800.30	740.45	736.60
Stripline End (IGBT's)	936.61	943.80	899.89	943.20	1229.7	1231.3	1177.1	1240.9

Appendix 2

Pulse Wave Approximation (30th place expansion)

```
clear all; close all; clc
format short

time = sym('time');

digits(5)
vpa((150000*.00005/.0005)...
+(2*150000/(1*3.14))*sin(1*3.14*(1/.0005)*.00005)*cos(1*2*3.14*(1/.0005)*time)...
+(2*150000/(2*3.14))*sin(2*3.14*(1/.0005)*.00005)*cos(2*2*3.14*(1/.0005)*time)...
+(2*150000/(3*3.14))*sin(3*3.14*(1/.0005)*.00005)*cos(3*2*3.14*(1/.0005)*time)...
+(2*150000/(4*3.14))*sin(4*3.14*(1/.0005)*.00005)*cos(4*2*3.14*(1/.0005)*time)...
+(2*150000/(5*3.14))*sin(5*3.14*(1/.0005)*.00005)*cos(5*2*3.14*(1/.0005)*time)...
+(2*150000/(6*3.14))*sin(6*3.14*(1/.0005)*.00005)*cos(6*2*3.14*(1/.0005)*time)...
+(2*150000/(7*3.14))*sin(7*3.14*(1/.0005)*.00005)*cos(7*2*3.14*(1/.0005)*time)...
+(2*150000/(8*3.14))*sin(8*3.14*(1/.0005)*.00005)*cos(8*2*3.14*(1/.0005)*time)...
+(2*150000/(9*3.14))*sin(9*3.14*(1/.0005)*.00005)*cos(9*2*3.14*(1/.0005)*time)...
+(2*150000/(10*3.14))*sin(10*3.14*(1/.0005)*.00005)*cos(10*2*3.14*(1/.0005)*time)...
+(2*150000/(11*3.14))*sin(11*3.14*(1/.0005)*.00005)*cos(11*2*3.14*(1/.0005)*time)...
+(2*150000/(12*3.14))*sin(12*3.14*(1/.0005)*.00005)*cos(12*2*3.14*(1/.0005)*time)...
+(2*150000/(13*3.14))*sin(13*3.14*(1/.0005)*.00005)*cos(13*2*3.14*(1/.0005)*time)...
+(2*150000/(14*3.14))*sin(14*3.14*(1/.0005)*.00005)*cos(14*2*3.14*(1/.0005)*time)...
+(2*150000/(15*3.14))*sin(15*3.14*(1/.0005)*.00005)*cos(15*2*3.14*(1/.0005)*time)...
+(2*150000/(16*3.14))*sin(16*3.14*(1/.0005)*.00005)*cos(16*2*3.14*(1/.0005)*time)...
+(2*150000/(17*3.14))*sin(17*3.14*(1/.0005)*.00005)*cos(17*2*3.14*(1/.0005)*time)...
+(2*150000/(18*3.14))*sin(18*3.14*(1/.0005)*.00005)*cos(18*2*3.14*(1/.0005)*time)...
+(2*150000/(19*3.14))*sin(19*3.14*(1/.0005)*.00005)*cos(19*2*3.14*(1/.0005)*time)...
+(2*150000/(20*3.14))*sin(20*3.14*(1/.0005)*.00005)*cos(20*2*3.14*(1/.0005)*time)...
+(2*150000/(21*3.14))*sin(21*3.14*(1/.0005)*.00005)*cos(21*2*3.14*(1/.0005)*time)...
+(2*150000/(22*3.14))*sin(22*3.14*(1/.0005)*.00005)*cos(22*2*3.14*(1/.0005)*time)...
+(2*150000/(23*3.14))*sin(23*3.14*(1/.0005)*.00005)*cos(23*2*3.14*(1/.0005)*time)...
+(2*150000/(24*3.14))*sin(24*3.14*(1/.0005)*.00005)*cos(24*2*3.14*(1/.0005)*time)...
+(2*150000/(25*3.14))*sin(25*3.14*(1/.0005)*.00005)*cos(25*2*3.14*(1/.0005)*time)...
+(2*150000/(26*3.14))*sin(26*3.14*(1/.0005)*.00005)*cos(26*2*3.14*(1/.0005)*time)...
+(2*150000/(27*3.14))*sin(27*3.14*(1/.0005)*.00005)*cos(27*2*3.14*(1/.0005)*time)...
+(2*150000/(28*3.14))*sin(28*3.14*(1/.0005)*.00005)*cos(28*2*3.14*(1/.0005)*time)...
+(2*150000/(29*3.14))*sin(29*3.14*(1/.0005)*.00005)*cos(29*2*3.14*(1/.0005)*time)...
+(2*150000/(30*3.14))*sin(30*3.14*(1/.0005)*.00005)*cos(30*2*3.14*(1/.0005)*time))
```

Convection Constant Curve Datapoints

```
clear all; close all; clc
%%%%%%%%%%%%%%%%User changable stuff%%%%%%%%%%%%%%%%
L = 0.23; %Characteristic vertical length (m)
Tinf = 22; %Ambient Temperature (°C)
%%%%%%%%%%%%%%%%%%%%%%%%%%%%%%%%%%%%%%%%%%%%%%%%%%%%

T = linspace(Tinf,300,800);

k = 0.02587; %Thermal Conductivity of air in (W/m·K)
beta = 0.0034; %Thermal expansion coefficient (1/K)
g = 9.81; %Gravitational acceleration (m/s^2)
nu = 0.0000185; %Kinematic viscosity (kg/m·s)
rho = 101325/(287.058*(Tinf + 273.15)); %Density (kg/m^3)
cp = 1.007*10^3; %Specific heat capacity (m^2/s)

alpha = k/(rho*cp); %Thermal diffusivity

Ra = (g*beta/(nu*alpha))*(T-Tinf)*L^3; %Rayleigh number
Pr = nu/alpha; %Prandtl number
```

```
h = zeros(length(Ra),1);
for i = 1:length(Ra)
    if Ra(i) < 10^9
        h(i) = (k/L)*(0.68 + (0.67*Ra(i)^(1/4))/(1+(0.492/Pr)^(9/16))^(4/9));
    else
        h(i) = (k/L)*(0.825 + (0.387*Ra(i)^(1/6))/(1+(0.492/Pr)^(9/16))^(8/27))^2;
    end
end

AnsysOutput = horzcat(T',h);

plot(T,h,'linewidth',2)
xlabel('Temperature')
ylabel('Convection Coefficient')
```